Characteristics of Kelvin-Helmholtz Waves as Observed by the MMS from September 2015 to June 2017

Rachel Rice[1], **Katariina Nykyri**[1], **Xuanye Ma**[1]

[1]Embry-Riddle Aeronatutical University, Department of Physical Sciences, Center for Space and Atmospheric Research

Key Points:

- A survey of MMS data from September 2015 to June 2017 identified 19 Kelvin-Helmholtz wave events.
- KH events are only observed for solar wind speed between 300−600 km/s. KHI growth rates are otherwise independent of solar wind conditions.
- New methods are developed for the automatic detection of magnetosheath and magnetospheric regions within the KHI.

Corresponding author: Rachel Rice, `ricer4@my.erau.edu`

Abstract

The Magnetospheric Multiscale (MMS) mission has presented a new opportunity to study the fine scale structures and phenomena of Earth's magnetosphere, including cross scale processes associated with the Kelvin-Helmholtz Instability (KHI). We present an overview of 19 MMS observations of the KHI from September 2015 to June 2017. Unitless growth rates and unstable solid angles for each of the 19 events were calculated using 5 techniques to automatically detect plasma regions on either side of the magnetopause boundary. There was no apparent correlation between solar wind conditions during the KHI and its growth rate and unstable solid angle, though we note no KHI were observed for solar wind flow speeds less than 300 km/s or greater than 600 km/s, likely due to a filtering effect of the instability onset criteria and plasma compressibility. Two-dimensional Magnetohydrodynamic (2D MHD) simulations were compared with two of the observed MMS events. Comparison of the observations with the 2D MHD simulations indicates that velocity dependent methods are the most consistent when calculating growth rate and unstable solid angle, but a combination of the velocity dependent and independent methods can be used to select KHI events in which the vortex has rolled over. This may prove useful for future work studying secondary processes associated with the KHI.

1 Introduction

The coupling of the solar wind (SW) to Earth's magnetosphere and its impacts on local space weather are a fundamental question of space physics. Several mechanisms operating at the magnetopause boundary, such as magnetic reconnection [*Paschmann et al.*, 1979; *Sonnerup et al.*; *Gosling et al.*, 1986; *Burch and Phan*, 2016] and viscous interactions [*Axford and Hines*, 1961; *Otto and Fairfield*, 2000; *Fairfield et al.*, 2000], are responsible for the transfer of mass and energy from the solar wind to the magnetosphere. Understanding the detailed effects of these processes is vital to predict and help prevent negative outcomes from space weather.

Observations from Defense Meteorological Satellite Program (DMSP) and Time History of Events and Macroscale Interactions during Substorm (THEMIS) spacecraft have established that the cold component ions of the plasma sheet are 30-40% hotter in the dawn flank than in the dusk [*Hasegawa et al.*, 2003; *Wing et al.*, 2005; *Dimmock et al.*, 2015]. *Dimmock et al.* [2015] conducted a statistical study of the magnetosheath source population as observed by THEMIS spacecraft over seven years, which showed ions in

the dawn flank are on average 10% hotter than those in the dusk flank. This asymmetry is more pronounced under fast ($>$ 400 km/s) SW conditions [*Dimmock et al.*, 2015]. However, even during fast SW, the asymmetry of the magnetosheath source plasma is insufficient to produce the observed asymmetry in the plasma sheet. MHD simulations were unable to reproduce the observed sheath asymmetry, but it was apparent in hybrid models, suggesting a kinetic scale mechanism is responsible for asymmetrically driving the heating of cold component ions in the sheath and further into the magnetosphere [*Dimmock et al.*, 2015].

Several physical mechanisms have been proposed as drivers of the observed plasma sheet asymmetry. Kelvin-Helmholtz instabilities (KHI), which occur regularly at the magnetopause boundary, are one such mechanism [*Otto and Fairfield*, 2000; *Fairfield et al.*, 2000; *Nykyri et al.*, 2003; *Hasegawa et al.*, 2004; *Nykyri et al.*, 2006; *Taylor et al.*, 2008; *Foullon et al.*, 2008; *Merkin et al.*, 2013; *Lin et al.*, 2014; *Ma et al.*, 2014a,b; *Nykyri et al.*, 2017; *Ma et al.*, 2017; *Sorathia et al.*, 2019]. KHI occur in regions of large shear flow [*Chandrasekhar*, 1961], such as the boundary between magnetosheath plasma flowing with the shocked SW and the relatively stagnant magnetosphere [*Miura and Pritchett*, 1982]. Long established as a source for momentum and energy transport from the SW to the magnetosphere [*Miura*, 1984, 1987], later simulations and observations have shown non-linear stages of the KHI are also capable of reconnection [*Nykyri and Otto*, 2001, 2004; *Nykyri et al.*, 2006; *Hasegawa et al.*, 2009] and ion heating via kinetic wave modes within the vortices [*Moore et al.*, 2016, 2017]. Compressional waves, like the Kelvin-Helmholtz or ultra-low frequency (ULF) waves, can also lead to kinetic Alfvén wave (KAW) generation via mode conversion [*Johson et al.*, 2001; *Chaston et al.*, 2007]. Recent work has suggested that KAWs associated with the KHI can contribute to parallel electron heating, but are insufficient to account for the total heating [*Nykyri et al.*, 2020]. A detailed mechanism for the KHI to develop electron scale waves and quantifying their contribution to electron heating is still an open question.

Observations have shown the the KHI may form on both the dawn and dusk flanks under any orientation of the interplanetary magnetic field (IMF) [*Kavosi and Reader*, 2015], but simulations have shown a preference for dawn flank formation when the IMF is in a Parker Spiral (PS) orientation [*Nykyri*, 2013; *Adamson et al.*, 2016]. Recent work by *Henry et al.* [2017] analyzed the events presented in *Kavosi and Reader* [2015] and confirmed this preference observationally. *Henry et al.* [2017] also confirmed a preference

for KHI formation at the dusk flank for high solar wind speeds under northward IMF (NIMF). As PS is the most statistically common IMF orientation, it follows that the associated preference for dawn-side KHI development would also be statistically more common. Such asymmetry in the formation of KHI, combined with KH-driven secondary processes like reconnection and kinetic scale waves, make the KHI a strong candidate to drive the dawn-dusk asymmetry of cold-component ions in the plasma sheet.

The launch of the Magnetospheric Multiscale (MMS) satellites presents a new opportunity to extend this study of the KHI and its associated secondary processes to smaller scales with higher resolution measurements. Within months of its launch, MMS had encountered KHI [*Eriksson et al.*, 2016]. The event reported by *Eriksson et al.* [2016] has been the subject of several case studies: *Li et al.* [2016] found evidence of Alfvénic ion jets and electron mixing due to reconnection at the trailing edge of the vortex; *Wilder et al.* [2016] noted compressed current sheets and evidence of ion-acoustic waves, and *Stawarz et al.* [2016] took advantage of MMS's high temporal and spatial resolutions to study turbulence generated by the KHI. These secondary processes would contribute to ion heating and plasma transfer across the magnetopause boundary.

In order to better understand the role KHI and its secondary process play in driving the plasma sheet asymmetry it is imperative, as a first step, to build a database of MMS encounters with KHI. The location, duration, and prevailing IMF conditions of each event are correlated with the unitless growth rates to establish patterns which may prove informative in understanding the role KHI plays in magnetospheric dynamics (e.g., in generating dawn-dusk asymmetries via secondary,"cross-scale" processes or affecting the radiation belt electron populations via ULF wave generation or magnetopause shadowing).

In this paper we present a list of MMS encounters with KHI and the physical characteristics of each. The MMS instrumentation and observational signatures used to identify the KHI encounters are described in Sections 2.2-2.3. Section 2.4 details the methodology used to separate magnetosheath and magnetospheric regions of the observed events, typical parameters of which were used in calculation of the unitless growth rate and unstable solid angle for each event. These methodologies were also tested using 2-dimensional magnetohydrodynamic simulations as described in Section 3. Results and conclusions are presented and discussed in Section 4.

2 Methodology

2.1 MMS Instrumentation

Obserational data reported here is level 2 data from MMS 1 [*Burch et al.*, 2016]. Spacecraft separations are at most 230 km, and more typically on the order of 20 km, well below the typical size of the KHI, thus all spacecraft are expected to observe the same signatures and a single craft is sufficient to identify the KHI. Ion energy spectra and moments are taken from the Fast Plasma Investigation (FPI) [*Pollock et al.*]. The Flux Gate Magnetometers (FGM) were used for the DC magnetic field [*Russell et al.*; *Torbet et al.*, 2016]. Data file versions used are v3.3.0.cdf for FPI and v4.18.0.cdf for FGM. Solar wind data are taken from the OMNI database [*King and Papitashvili*, 2005].

2.2 Observational Signatures of the KHI

KHI are known to occur at regions of large velocity shear, such as at the flank magnetopause. In this region the magnetosphere is relatively stagnant and plasma in the sheath is accelerating from low speeds immediately after the shock to "catch up" with the solar wind speed downtail [*Dimmock and Nykyri*, 2013]. At this boundary MMS observes a rapid change in ion bulk velocity on the order of several 100's of km/s. This change in bulk velocity, however, is characteristic of most boundary crossings even if the boundary is stable. An unstable boundary, which MMS may cross several times, exhibits quasi-periodic fluctuations in ion energies between typical magnetosheath and magnetospheric values. Similarly, anti-correlated quasi-periodic signatures are also observed in the ion temperature and density for an unstable boundary. To distinguish the KHI from a shifting boundary (as a response to SW dynamic pressure variations) or other boundary instabilities (such as flux transfer events (FTE)), MMS is expected to observe quasi-periodic magnetic field fluctuations, particularly in the component of the field normal to the boundary, which indicate twisting of the field lines within the KH vortex. Total field strength will also vary due to compressions by the KHI. The vortex nature of the KHI also creates a force imbalance as the rotational motion creates outward force. This is balanced by a pressure gradient such that a decrease of total pressure is observed at the center of the vortex. Potential KHI events thus show a lower total pressure near the center of the vortex (where $\mathbf{B_N}$ is zero) and higher pressure in the spine region, whereas FTEs

are typically associated with an increase in total pressure when $\mathbf{B_N}$ is zero [*Nykyri et al.*, 2006; *Zhao et al.*, 2016].

Table 1 summarized the 19 MMS encounters of the KHI. Events are evenly distributed between the dawn (9) and dusk (10) flanks. Only two events occur well into the tail, the other 17 are observed sunward of the terminator. This is primarily due to a sampling effect of the MMS phase 1 orbit which targeted dayside magentopause. Encountered events ranged in duration from as little as 15 minutes to over 2 hours. Examples of two of the listed events (marked with asterisks) are shown in Figures 1 and 2.

Table 2 details the prevailing SW conditions for each event. At the time of event onset, IMF configurations are well distributed between Parker spiral (4), northward (3), southward (3), radial (4), dawnward (2), and duskward (3) orientations. However, for the duration of each event, average IMF configurations show a slight preference for the Parker spiral orientation (6), followed by radial and duskward (4 each), northward and southward (2 each), and dawnward (1). None of the the observed events occurred under ortho-Parker Spiral IMF orientation. Solar wind flow speeds are never less than 300 km/s or greater than 600 km/s. Pressure is typically between 1.4 and 3.5 nPa, with only one event occurring outside this range, with solar wind pressure 5 nPa. Solar wind parameters are discussed in more detail and correlated with the KHI growth rate in Section 4.

Figure 1 shows MMS1 observations of ions from 06:00 to 07:00 on 15 October 2015. MMS passed through the dusk side of the dayside mangnetopause during strongly dawnward IMF. The omni-directional ion energy spectrogram in panel (a) shows the expected quasi-periodic variations throughout the interval. The magnetic field in panel (b) shows fluctuations characteristic of the KHI from 06:20 to 06:40 and again near 06:50. A velocity shear on the order of 200 km/s is visible near 06:25 in panel (c) and anti-correlated fluctuations of ion density and temperature, shown in panel (d), occur throughout the interval. Decreases in total pressure, shown in black in panel (e), are visible starting around 06:20.

MMS observations of another KHI encounter on 26 September 2016 are shown in Figure 2 for the 70 minutes from 14:15 to 15:25. MMS crossed the dusk flank magnetopause while the IMF was in a Parker Spiral orientation. Quasi-periodic fluctuations in omni directional ion spectra are observable from approximately 14:20 to 15:15 in panel

Table 1. MMS observed 19 KHI from September 2015 to June 2017. The duration and GSM location of each event are listed. Events were observed equally on the dawn and dusk flanks. The shortest encounter lasted only 10 minutes, and the longest were 130 minutes. Observations for marked (*) events are shown in Figures 1 and 2

Date	Onset Time (UT)	Duration (min)	GSM Location (R_E) X	Y	Z
08 Sep 2015	09:20	130	5.0	7.8	-4.5
11 Oct 2015	10:35	20	8.7	6.5	-4.7
*15 Oct 2015	06:05	45	9.0	4.1	-2.3
17 Oct 2015	16:05	22	6.4	7.8	-4.1
18 Oct 2015	15:05	15	7.2	7.5	-4.4
22 Dec 2015	22:20	25	7.9	-5.7	-1.8
11 Jan 2016	20:56	10	6.2	-7.6	-3.4
22 Jan 2016	19:40	40	5.0	-8.5	-5.2
05 Feb 2016	19:00	25	3.3	-9.3	-5.0
07 Feb 2016	03:55	35	7.0	-6.9	-3.5
18 Feb 2016	19:30	55	2.5	-9.7	-6.3
25 Feb 2016	18:55	70	1.3	-9.9	-6.5
*26 Sep 2016	14:30	45	2.7	8.5	-5.4
04 Oct 2016	18:40	40	1.8	11.2	-3.6
10 Oct 2016	14:50	40	4.3	9.3	-5.0
24 Oct 2016	10:55	20	6.8	6.1	-4.3
04 Nov 2016	12:00	50	8.1	7.2	-3.8
03 May 2017	02:10	130	-12.9	-19.7	-3.9
11 May 2017	12:45	70	-15.6	-18.3	1.3

163 **Table 2.** MMS observed 19 KHI from September 2015 to June 2017. Onset and average IMF
164 orientations and solar wind Alfvén Mach number are determined using OMNI data.

Date	Onset IMF Angles (deg)		Average IMF Angles (deg)		Flow	Alfvén	Pressure
	Clock	Cone	Clock	Cone	Speed (km/s)	Mach Number	(nPa)
08 Sep 2015	12.6	50.6	22.0	52.3	509.2	3.8	5.2
11 Oct 2015	-56.4	123.5	-48.4	111.7	478.0	10.9	1.4
15 Oct 2015	-82.9	92.5	-67.5	94.7	482.7	7.4	1.6
17 Oct 2015	82.2	128.6	-88.8	126.5	345.6	11.5	3.5
18 Oct 2015	-178.6	128.0	-51.1	146.3	454.6	10.5	2.0
22 Dec 2015	-96.9	65.3	129.6	35.8	411.4	7.6	2.0
11 Jan 2016	-113.4	77.8	-116.7	87.8	583.4	4.6	1.7
22 Jan 2016	26.7	15.7	0.5	6.0	493.4	6.3	1.5
05 Feb 2016	-25.7	125.6	-50.5	121.9	470.4	9.4	1.7
07 Feb 2016	42.7	83.4	36.0	78.0	405.3	11.1	2.4
18 Feb 2016	104.3	24.5	-175.1	48.0	594.9	10.2	2.0
25 Feb 2016	-145.6	146.4	-135.0	147.6	302.9	6.5	3.2
26 Sep 2016	-66.0	130.3	-54.6	107.4	430.8	6.8	3.2
04 Oct 2016	-30.0	145.4	86.8	151.7	532.6	9.6	3.2
10 Oct 2016	-86.0	112.5	-62.3	107.7	355.0	9.0	3.0
24 Oct 2016	-15.1	85.4	-21.4	88.7	383.5	9.8	3.5
04 Nov 2016	23.1	120.7	58.8	121.8	370.2	7.6	1.4
03 May 2017	51.4	137.6	49.6	139.7	414.1	14.8	1.4
11 May 2017	60.0	88.6	56.7	81.7	361.4	6.8	2.5

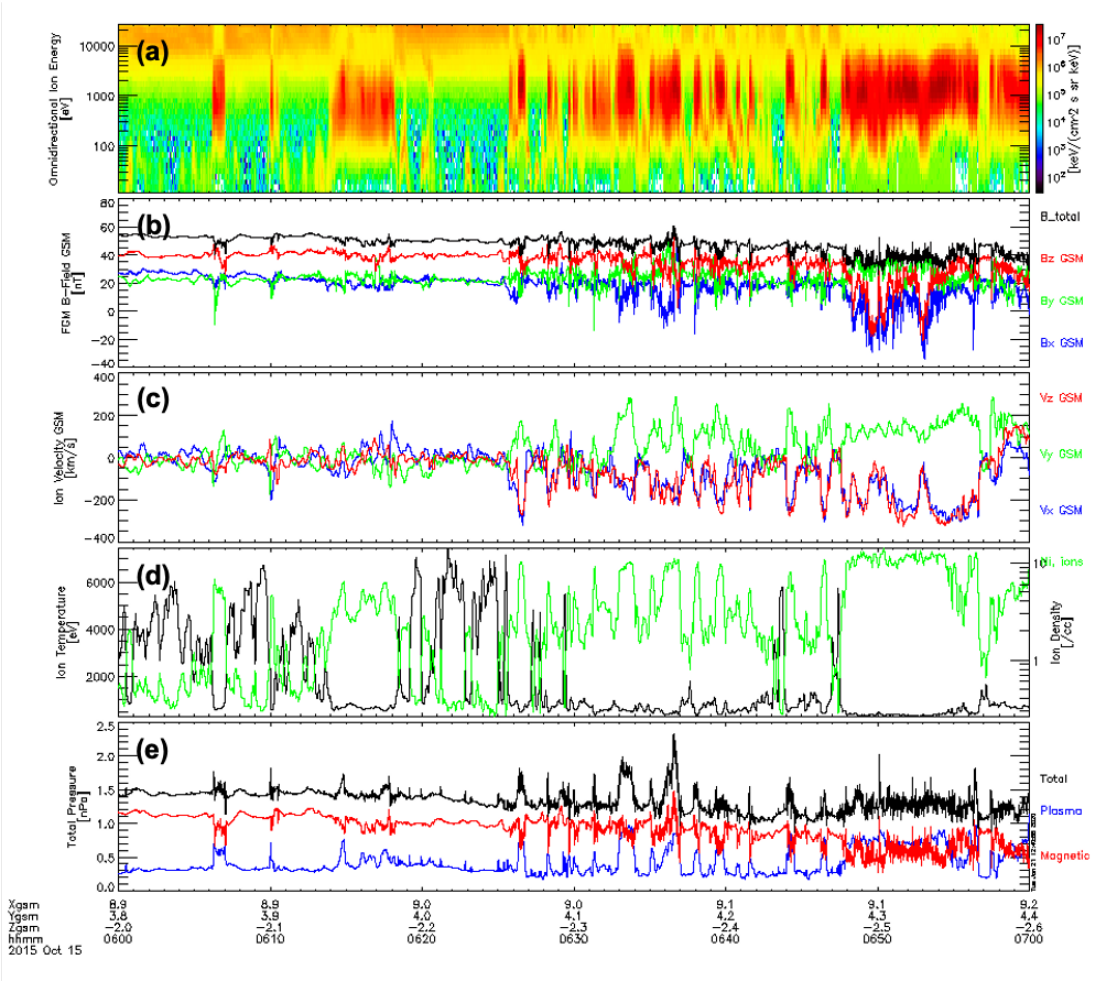

Figure 1. MMS observations of (a) omnidirectional ion energies; (b) magnetic field in GSM coordinates; (c) ion bulk velocity in GSM coordinates; (d) ion temperature and density; and (e) total, magnetic and plasma pressures from 06:00 to 07:00 UT on 15 October 2015. Ion data is taken from the Fast Plasma Investigation (FPI) and magnetic field data is from the Flux Gate Magentometer (FGM) aboard MMS1.

(a) and are accompanied by anti-correlated variations in ion density and temperature (d). Velocity shears (c) on the order of 150-200 km/s occur several times from 14:20 to 15:20. Panel (b) shows fluctuations around 20 nT and up to 40 nT in the magnetic field. Decreases in total pressure are small, but observable in panel (e) from 14:35 to 15:10.

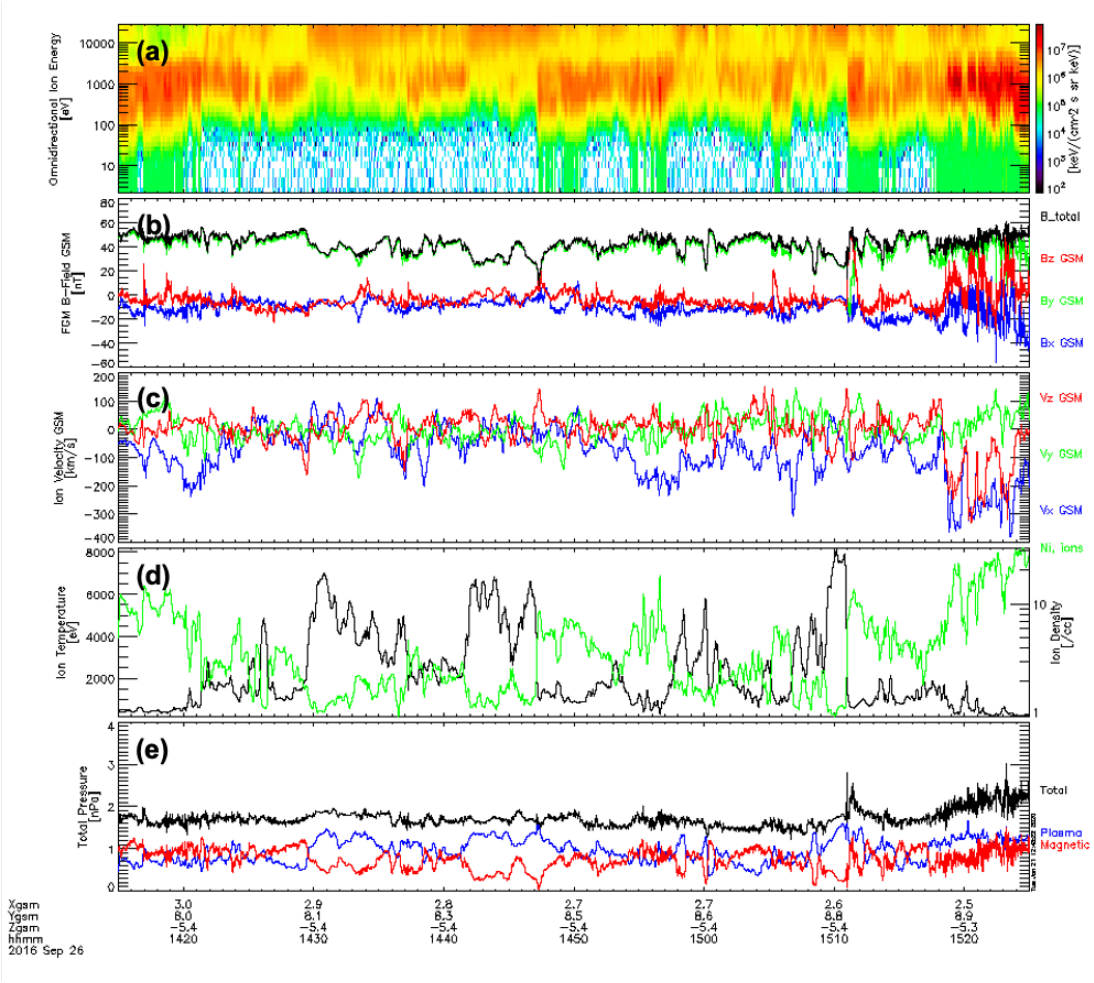

187 **Figure 2.** MMS observations as in Figure 1 from 14:15 to 15:25 UT on 26 September 2016.
188 Ion data is taken from the Fast Plasma Investigation (FPI) and magnetic field data is from the
189 Flux Gate Magentometer (FGM) aboard MMS1.

190 ### 2.3 Boundary Normal Coordinate System

191 It is useful to rotate observed data into boundary normal (LMN) coordinates for
192 further analysis. We make use of the maximum variance of the $\mathbf{v}\times\mathbf{B}$ electric field (MVAE)
193 technique to determine the average outward pointing normal direction, $\mathbf{N}$ for the full du-
194 ration of each event. The general method for variance analysis techniques is given in *Son-*
195 *nerup and Scheible* [1998]. *Nykyri et al.* [2011a,b] showed the single spacecraft MVAE
196 technique is sufficient for identification of the boundary normal direction when the plasma
197 bulk velocity and magnetic field are primarily tangential to the boundary, as is typically
198 in the case during KHI. It is also used here, rather than a multi-spacecraft method, to

allow for automation of the analysis. For MVAE, the direction in which the electric field variance is maximized (i.e., the direction of the maximum eigenvector of the MVAE matrix) is taken as the normal direction. Tangential directions are defined by the intermediate and minimum eigenvectors of the MVAE matrix, but are not included here. We use the eigenvalues associated with the maximum and intermediate eigenvectors to determine if the normal direction is well-determined. For a large maximum to intermediate eigenvalue ratio, $\lambda_{max}/\lambda_{int} > 5$, the normal is clearly determined. Smaller ratios indicate more ambiguity in the normal direction.

In Table 3 the average normal direction and eigenvalue ratio for each event are presented. Roughly half (9) of the events have a clear, well determined normal direction. Another two events have only moderately well determined normals ($\lambda_{max}/\lambda_{int} = 4.9$). The remaining 8 events are ambiguous in their normal direction. Events marked with an asterisk are examples shown in Figures 3 and 4

MVAE analysis also assists in determining how non-linear the KHI may be. Local normal directions, $\mathbf{n}$ are calculated every 15 seconds for 1-minute sliding windows for the duration of each event. The dot product, $\mathbf{n}\cdot\mathbf{N}$, is used to compare the average and local normal directions. For parallel $\mathbf{n}$ and $\mathbf{N}$, $\mathbf{n} \cdot \mathbf{N} = 1$, and there is no twisting of the boundary layer. As the boundary layer is twisted in the non-linear KHI $\mathbf{n} \cdot \mathbf{N} \rightarrow -1$. The local normal is not required to be outward pointing, but the shift from an outward to inward pointing normal is expected to be gradual [*Nykyri et al.*, 2006]. Sudden shifts are most likely due to the 180 degree ambiguity in the MVAE technique.

The 15th October 2015 event is shown in boundary normal coordinates from 06:00 to 07:00 in Figure 3. After rotating to the LMN system, the normal component of the magnetic field showed strong fluctuations, on the order of 20-40 nT (a). For this event the normal direction was was (0.779,0.266,-0.568) in GSM, which was well determined with an eigenvalue ratio of 10.401. Figure 3 shows evidence of boundary twisting from 06:00 to 06:40 (b). The boundary normal direction for each window was well determined, as shown by large value of the maximum to intermediate eigenvalue ratio (c). Because the average and local normal directions are all well-determined throughout the interval, this event is probably in a non-linear stage of development.

Figure 4 shows the KHI encounter from 14:15 to 15:25 on 26 September 2016 in boundary normal coordiates. Fluctuations of 20-40 nT in the normal magnetic field com-

Table 3. The outward pointing normal to the boundary layer is identified as the direction of maximum variance in the $\mathbf{v} \times \mathbf{B}$ electric field. This direction is well determined when the maximum eigenvalue significantly larger than the intermediate eigenvalue, yielding an eigenvalue ratios of 5 or greater.

Date	GSM Location (R_E)			Boundary Normal Direction			Average
	X	Y	Z	X	Y	Z	Eigenvalue Ratio
08 Sep 2015	5.0	7.8	-4.5	0.67	0.56	0.50	19.3
11 Oct 2015	8.7	6.5	-4.7	0.81	0.35	-0.47	8.8
15 Oct 2015	9.0	4.1	-2.3	0.78	0.27	-0.57	10.4
17 Oct 2015	6.4	7.8	-4.1	0.80	0.44	-0.40	3.9
18 Oct 2015	7.2	7.5	-4.4	0.80	0.35	-0.49	13.7
22 Dec 2015	7.9	-5.7	-1.8	0.78	-0.34	-0.53	4.9
11 Jan 2016	6.2	-7.6	-3.4	0.65	-0.40	-0.65	7.5
22 Jan 2016	5.0	-8.5	-5.2	0.56	-0.40	-0.72	1.6
05 Feb 2016	3.3	-9.3	-5.0	0.50	-0.50	-0.71	1.5
07 Feb 2016	7.0	-6.9	-3.5	0.86	-0.34	-0.39	3.8
18 Feb 2016	2.5	-9.7	-6.3	0.42	-0.39	-0.82	3.0
25 Feb 2016	1.3	-9.9	-6.5	0.54	-0.63	-0.56	14.4
26 Sep 2016	2.7	8.5	-5.4	0.48	0.32	-0.81	2.0
04 Oct 2016	1.8	11.2	-3.6	0.52	0.64	-0.57	2.6
10 Oct 2016	4.3	9.3	-5.0	0.72	0.48	-0.50	4.9
24 Oct 2016	6.8	6.1	-4.3	0.80	0.33	-0.49	13.5
04 Nov 2016	8.1	7.2	-3.8	0.78	0.38	-0.49	2.9
03 May 2017	-12.9	-19.7	-3.9	0.22	-0.95	-0.23	5.1
11 May 2017	-15.6	-18.3	1.4	0.18	-0.97	0.14	9.6

ponent are clear throughout the interval (a). The average normal direction for this event is (0.484,0.323,-0.813) in GSM. Given a 1.993 eigenvalue ratio, the average normal direction is not clearly determined. Panel (b) of Figure 4 shows twisting of the local boundary away from the average normal at semi-regular intervals for the the duration of the event. Local normals are generally well determined, as shown by eigenvalue ratios consistently on the oder of 10-100 (c).

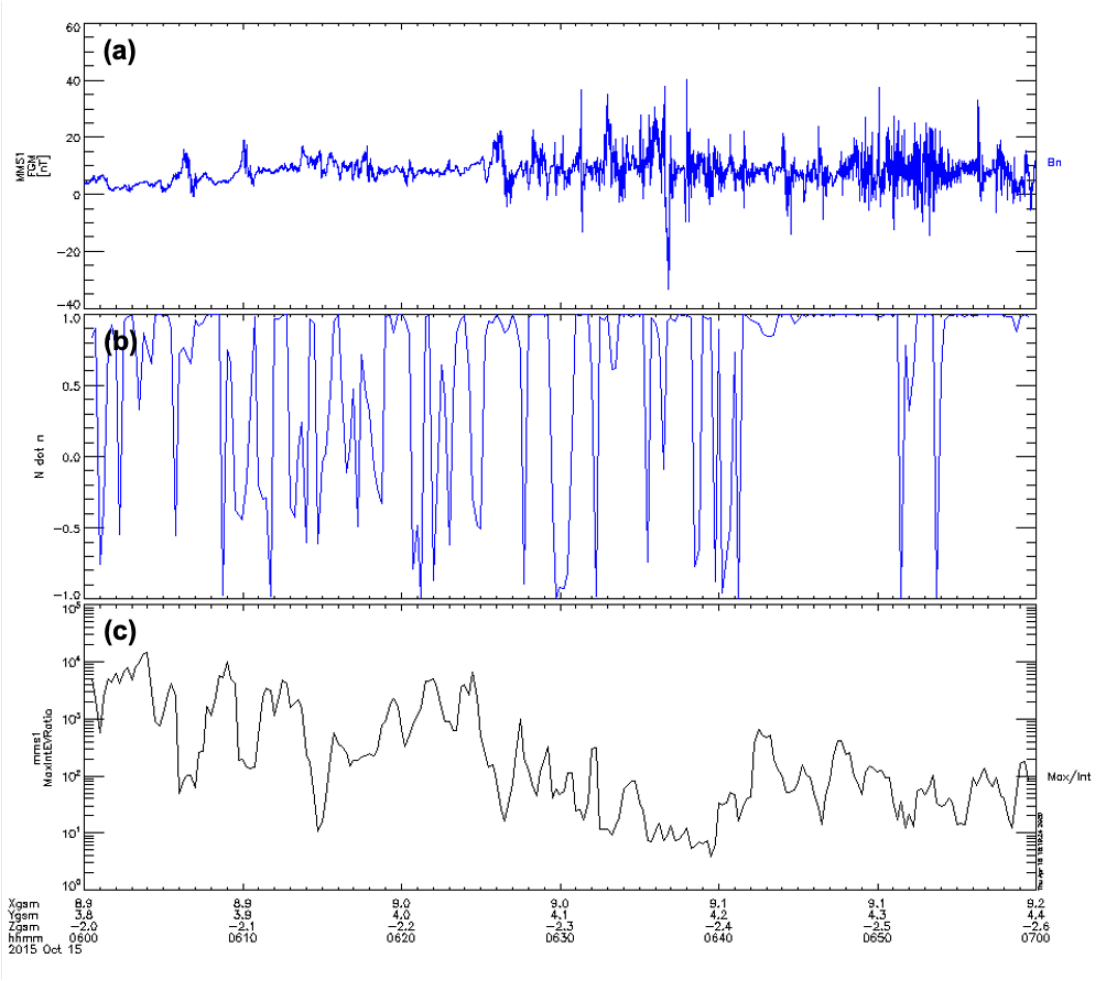

Figure 3. The (a) normal component of the magnetic field, (b) dot product of local and average normal directions, and (c) ratio of maximum and intermediate eigenvalues for each local window are derived from MMS1 FGM and FPI observations from 06:00 to 07:00 on 15 October 2015.

Having identified MMS encounters with the KHI, we next calculate the growth rates of the events and compare them with the prevailing solar wind and IMF properties.

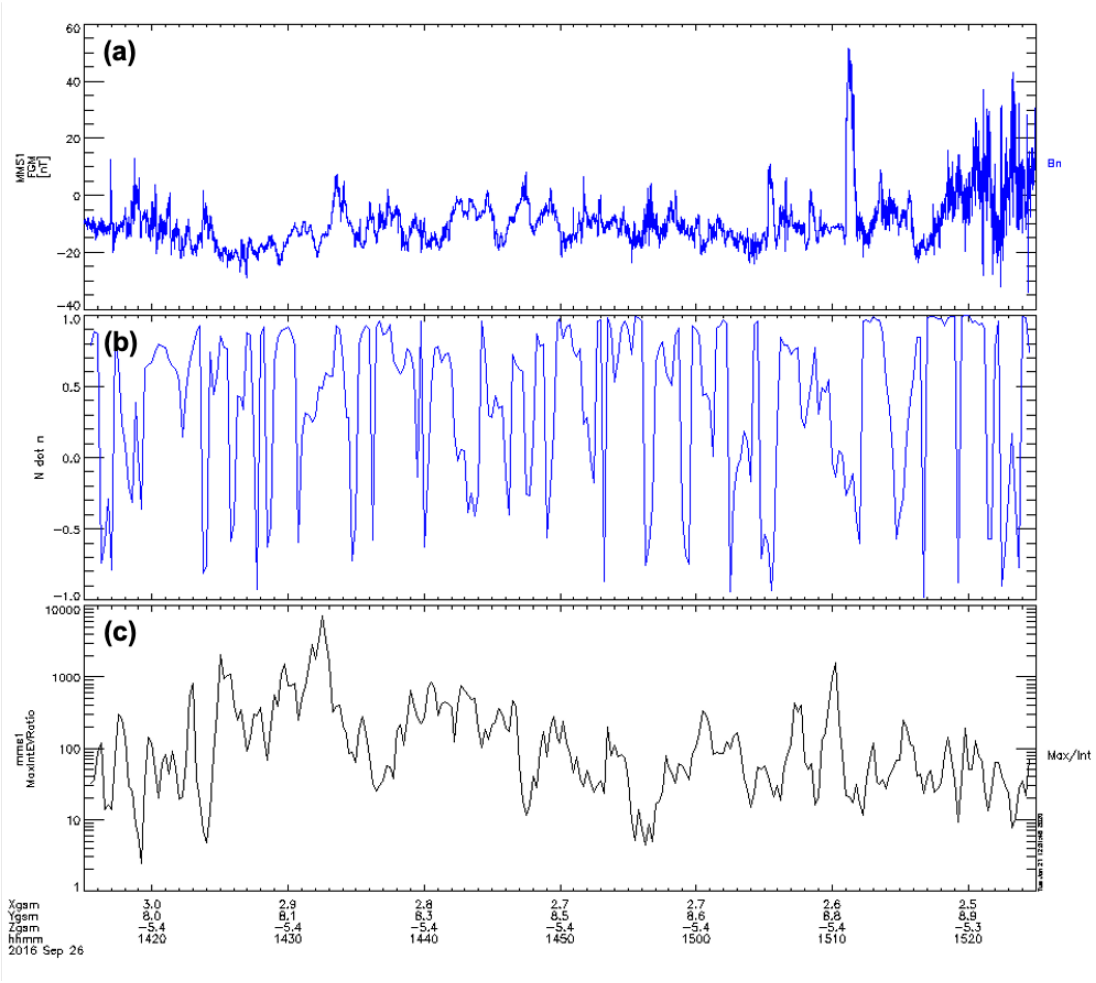

Figure 4. Quantities, as in Figure 3, are derived from MMS1 FGM and FPI observations from 14:15 to 15:25 on 126 September 2016.

2.4 Calculation of the Instability Growth Rate

Any region unstable to the KHI will satisfy the KHI instability criteria

$$[\mathbf{k}\cdot(\mathbf{v_1}-\mathbf{v_2})]^2 \geq \frac{n_1+n_2}{4\pi m_0 n_1 n_2}[(\mathbf{k}\cdot\mathbf{B_1})^2+(\mathbf{k}\cdot\mathbf{B_2})^2] \quad (1)$$

where $\mathbf{v_i}$, n_i, and $\mathbf{B_i}$ are the the velocity, density, and magnetic field on either side of the velocity shear layer and $\mathbf{k}$ is the wave vector [*Chandrasekhar*, 1961]. Note this equation is merely an approximation of the instability for an observed event as it assumes an infinitely thin boundary layer which is not true for the magnetopause. Equation 1 also assumes an incompressible plasma, yet for high ($>$ 600 km/s) solar wind speeds, the compressibility is sufficient to stabilize the development of the KHI. Furthermore, MMS will not necessarily observe the source region of the KHI gand local conditions may not match

those of the source region. Equation 1 may be rearranged to determine the normalized growth rate of the KHI in a particular region, which is defined as

$$Q/k = \sqrt{a_1 a_2(\mathbf{\Delta v}\cdot\hat{\mathbf{k}})^2 - a_1(\mathbf{v_{A1}}\cdot\hat{\mathbf{k}})^2 - a_2(\mathbf{v_{A2}}\cdot\hat{\mathbf{k}})^2} \tag{2}$$

where a_i is a density parameter for either side of the boundary defined by $a_i = \rho_i/(\rho_1+\rho_2)$, $\mathbf{v_{Ai}}$ is the Alfvén velocity on either side, and $\hat{\mathbf{k}}$ is the unit wave vector (thus the growth rate is normalized to the wavelength), pointing in the direction of maximum growth. In order to compare the normalized growth rates for KHI events observed at various locations and under a variety of SW and IMF conditions, we make it completely unitless via comparison with the local fast mode speed, $v_{fm} = \sqrt{v_A^2 + c_s^2}$. The fast mode speed is not equal in the magnetosheath (sub-index msh) and magnetosphere (sub-index msp) regions, so we normalize to the mean of the two, such that

$$Q_{unitless} = \frac{Q/k}{v_{fm}}$$

where $v_{fm} = \frac{1}{2}(v_{fmmsh} + v_{fmmsp})$.

In Equation 2 the direction of $\hat{\mathbf{k}}$ is chosen to maximize the normalized growth rate, but many directions of $\hat{\mathbf{k}}$ may satisfy the instability criteria. This range of angles capable of satisfying the instability criteria can be used to determine just how susceptible a region is to the development of KHI.

KHI may propagate in any direction $\hat{\mathbf{k}}$ for which Q/k is positive. If we express $\hat{\mathbf{k}}$ in terms of the spherical angles ϕ and θ, the percent of the 4π solid angle that satisfies the KHI instability criteria at a given location may be calculated. We use the term this percentage the "unstable solid angle." Events with larger growth rates and/or larger unstable solid angles are likely to be KHI.

Calculation of the unitless growth rate and unstable solid angle requires the identification of separate regions of magnetosheath and magnetospheric plasma on either side of the magnetopause boundary. The unpreturbed flank magnetosheath is characterized by cold, dense plasma flowing tailward at high speeds with the shocked SW. In contrast the magnetospheric plasma is hot, tenuous, and relatively stagnant. Using several combinations of density, temperature, and the X-component of the bulk velocity we developed five methods to separate data from the magnetosheath and magnetosphere regions, allowing automated growth rate calculations. The isolated data was then used to deter-

mine characteristic values of each region for calculation of the growth rate and unstable solid angle.

2.4.1 Density-Temperature Ratio Methods

Method 1 uses a ratio of the ion density and average temperature, n/T, to identify the separate regions. The largest 20% and smallest 20% of all n/T values in the observation interval are used to calculate a typical value of n/T value at the magnetopause boundary, n/T_{mp}, for each interval. In the cold and dense magnetosheath n/T is significantly greater than in the hot and tenuous magnetosphere, so regions with $n/T > 1.5n/T_{mp}$ or $n/T < .5n/T_{mp}$ are classified as the magnetosheath or magnetospheric regions, respectively. We avoid any ambiguous and mixed regions, thus only the plasma parameters of pristine magnetosheath and magnetosphere are used in calculation of the growth rate and unstable solid angle. The regions identified using this method are marked in yellow (magnetosheath) and blue (magnetosphere) in Figure 5 for the 15 October 2015 event and Figure 6 for the event on 26 September 2016.

Method 1 is appropriate for linear stages of the KHI, but may fail for non-linear stages. In cases of rolled-up, non-linear KHI, a portion of the magnetospheric plasma may be accelerated within the vortex and carried tailward with the magnetosheath. Acceleration within the late stage KHI cannot have a physical effect on the development and initial growth rate, but without constraining the velocity this accelerated plasma may be identified with the magnetosphere and affect the initial conditions used in calculations. To avoid this issue, the mean and standard deviation of the tailward (X-component) magnetosheath velocity are found, and the magnetospheric region is constrained to plasma with tailward flow at least one standard deviation slower than the mean sheath speed, such that $v_{Xmsp} < v_{Xmsh} - \sigma_{v_{Xmsh}}$. Portions of the previously identified magnetosphere that fulfill the criteria are marked in green in Figure 5 and 6 for the example events.

As can be seen in Figures 5 and 6 both Methods 1 and 2 identify only a small portion of the intervals as magnetosheath. MMS data does suggest the spacecraft spent less time in the sheath than in the magnetosphere, but the omnidirectional energy spectrogram (panels (c) in Figures 5 and 6) show several regions (6:20 to 6:41 in 5, 14:56 and 15:11 in 6) which appear to have sheath like populations that these methods classified as ambiguous and/or mixed. A much larger region is identified as the magnetosphere and

is only slightly reduced when we constrain the velocity signature of the region. This indicates the velocity constraint is useful in accounting for the effects of rolled-up of the vortex.

In both methods, mean values for velocity, magnetic field, and density in either region are used to calculate the unitless growth rate and unstable solid angle. Results of these calculations for all the of identified MMS KHI encounters may be found in Table 5 and Table 6.

2.4.2 Specific Entropy Methods

Method 3 uses the specific entropy, $S = T/n^{2/3}$, rather than n/T, to identify the regions on either side of the boundary layer. Again the largest and smallest 20% of all S values in an interval are used to determine the typical value at the magnetopause boundary, S_{mp}, for each event. The specific entropy of the magnetosheath is expected to be significantly less than the magnetosphere, so regions with $S < 0.5S_{mp}$ are sorted to the magnetosheath and regions with $S > 1.5S_{mp}$ are sorted to the magnetosphere. In this method, as with the density-temperature ratio methods, ambiguous and mixed regions are avoided when calculating characteristic parameters for each region. The sheath, as identified using the specific entropy, is marked in yellow in Figure 7 and 8 for the 15 October 2015 and 26 September 2016 events respectively; the magnetosphere is marked in blue.

As in the density-temperature ratio, identification of the sheath and magnetosphere using specific entropy does not consider the expected velocity differences in the regions, thus it may be less effective for rolled-up KHI vortices. Again we require the magnetospheric plasma be flowing tailward at least one standard deviation slower than the sheath ($v_{Xmsp} < v_{Xmsh} - \sigma_{v_{Xmsh}}$). The remaining magnetospheric regions meeting this constraint are marked in green in Figure 7 and 8.

Using this methodology, a much larger portion of each event is classified as magnetosheath plasma, including some intervals that appear mixed and ambiguous in the MMS data (6:30 to 6:43, 6:44 to 6:47 in Figure 7 and 14:47 to 14:58, 15:11 to 15:17 in Figure 8). The magnetosphere accounts for only a few minutes of the example events, in direct contradiction to the regions identified using the density-temperature ratio. Constraining the velocity required in the magnetosphere, reduces the region even further,

to the point MMS does not spend enough time in the region to calculate reliable plasma parameters.

Results for the growth rate and unstable solid angles using mean sheath and magnetosphere parameters as determined with both the unconstrained and velocity-constrained specific entropy methods are reported in Table 5 and Table 6.

2.4.3 Density and Velocity Method

The final method uses the product of density and tailward (GSE/GSM $X-$component) velocity, nv_x to separate regions of the sheath and magnetospheric plasma. As in all other methods, the mean of the largest and smallest 20% of nv_X values in the interval are used as the typical magnetopause value, nv_{Xmp}. In the shocked SW of the magnetosheath, nv_x is large and negative, while it is small in the stagnant magnetosphere. Thus the magnetosheath comprises regions of $nv_X < nv_{Xmp}$, and the magnetosphere comprises regions of $nv_X > nv_{Xmp}$. Mixed and ambiguous regions are not avoided in this method, thus the presence of a significant transition layer will affect the normalized growth rate. The sheath and magnetosphere identified using this method are marked in yellow and blue respectively for the 15 October 2015 event in Figure 9 and for the 26 September 2016 event in Figure 10.

Unlike the previous methods, mixed and ambiguous regions are intentionally included in this method. This avoids the exclusion of relevant intervals, but can also unpredictably affect the parameters used for the growth rate calculation. In both example cases only a small portion of the interval is classified as the magnetosheath and several regions, which exhibit sheath like characteristics, are instead sorted into the magnetosphere (6:06, 6:14 to 6:19 in Figure 9 and 14:48 to 14:52 in Figure 10).

Values of the unitless growth rate and unstable solid angle of all the events found using the density-velocity product are reported in Table 5 and Table 6.

Unitless growth rate is not a perfect parameter to describe the KHI. The KHI is a convective instability which dissipates stored energy as it develops, thus growth rate and the unstable solid angle are maximized just prior to the formation of the KHI. The nature of in-situ observations, however, dictates we cannot identify KHI until they are relatively well developed. Thus small growth rates and unstable solid angles are not nec-

essarily counter-indicative of KHI, but may instead be features of later stage KHI. As KHI develop, they may form non-linear vortices, which can be seen in observations as low density magnetospheric plasma flowing tailward with the magnetosheath [*Hasegawa et al.*, 2006; *Taylor et al.*, 2012]. Figure 11 plots tailward velocity as a function of ion density for the event on (top) 15 October 2015 and (bottom) 26 September 2016. Color overlays correspond with (left) the density temperature ratio, n/T; (center) specific entropy, S; and (right) the density-tailward velocity product nv_X. Red to orange points are magnetospheric values, blue to green are the sheath. As expected from Figures 5 and 6, the n/T parameter identifies only a few points in the sheath, and indicates a significant amount of the magnetospheric plasma moving tailward with the magnetosheath, as in a rolled up vortex. The specific entropy method, on the other hand indicates no magnetospheric plasma flows with the magnetosheath, but also indicates almost no magnetospheric plasma generally. The method using the product of the density and tailward velocity yields the largest mixed region of any of the methods, with only a small portion of the data identified as the magnetosheath. Any indication of a non-linear rolled-up vortex is obscured by the large number of mixed and ambiguous data points.

3 Comparison with Simulations

To verify our method for the calculation of normalized growth rates is robust it was applied to parameters generated by two dimensional MHD simulations of KHI. A simulation case for the KHI developing under Northward IMF (NIMF) conditions was tested using initial conditions comparable to those of the event on 08 September 2015. A second simulation case used initial conditions similar to those of the 18 October 2015 event for the KHI developing on the dusk flank under Parker Spiral IMF (PSIMF).

The simulations, after *Ma et al.* [2019], solve the full set of resistive Hall-MHD equations equations using a leapfrog scheme [*Potter*, 1973; *Birn*, 1980; *Otto*, 1990]. We normalize all physical quantities to their typical scale, for example, the length L is normalized to L_0, the half width of the initial sheered flow; number density to n_0, the magnetic field to B_0, velocity to the Alfvén velocity, $V_A = B/\sqrt{\mu_0 \rho_0}$; and the time to the Alfvén transit time. The values of the these normalizations for each simulation case are summarized in Table 4

425 **Table 4.** Normalization constants for the 2D MHD simulations.

Quantity	Northward	Parker spiral
Magnetic field B_0 (nT)	71.5	33.38
Number Density n_0 (/cc)	12.36	6.45
Length scale L_0 (km)	640	640
Velocity V_A (km/s)	443	286.5
Time t_0 (s)	1.35	2.23

426 A cut was taken through the KHI vortex in the simulation box every 10 time steps.
427 Data from these cuts was separated into distinct regions using the methods described
428 in Sections 2.4.1 - 2.4.3 and used to calculate growth rates and unstable solid angles. The
429 growth rates as a function of time are shown on the left of Figures 12 and 13 for the PSIMF
430 and NIMF cases respectively; examples of the density within the KHI and the cuts used
431 for calculations (red) are shown on the right. The "true" growth rate, as determined by
432 the linear slope of a plot of $ln(v_\perp)$ as a function of time, is also shown (solid black line).
433 In both cases, all methods overestimate the growth rate, which is expected as the cal-
434 culation assumes an infinitely thin boundary layer and incompressible plasma.

442 As can be seen in Figures 12 and 13 for the PSIMF and NIMF cases, respectively,
443 all methods produced very similar results until vortex roll-over was captured by the cut.
444 After roll-over occurred, the velocity-independent methods saw a sharp decrease in growth
445 rate. The velocity dependent methods remained roughly consistent throughout roll-over
446 and saw a more gradual decrease in growth rate as the instability dissipated. We do note
447 that the method using a product of density and tailward velocity behaved more unpre-
448 dictably than the other velocity dependent methods. This is likely due to the inclusion
449 of mixed and ambiguous regions with this method.

450 The unstable solid angle followed a similar pattern as the unitless growth rate, but
451 remained near its minimum value longer than the growth rate. Both simulation cases
452 produced a larger initial growth rates and unstable solid angles than the observational
453 events they were based on. As the the simulations progressed however, the growth rate
454 and unstable solid angle decreased to roughly match the observational case, and at later

simulation times, some methods produced unstable solid angles less than the MMS observations.

4 Conclusions and Discussion

The main conclusions may be summarized as follows:

- MMS observed 19 clear KHI events from September 2015 to June 2017.

From September 2015 to June 2017 MMS observed more than 80 mixed regions which initially resembled KHI. Further analysis of growth rate calculations, total pressure and boundary-normal rotated magnetic field showed 19 of these events likely to be KHI. These 19 events, summarized in Table 1, were evenly distributed between the dawn and dusk flanks and occur under a variety of prevailing SW conditions and IMF orientations.

- A method combining the density-temperature ratio and tailward velocity of a KHI event is most consistent at automatically identifying regions of magnetosheath and magnetospheric plasma for calculation of the KHI growth rate and unstable solid angle.

Five methods are developed to separate the sheath and magnetospheric regions in the MMS data. Mean parameters from each region are used to calculate the unitless growth rate and unstable solid angle for each of the 19 events. Results of the growth rate and unstable solid angle calculations for all methods are presented in Table 5 and Table 6 respectively. When the results of the calculations are considered with the identified regions, mean parameters of each region, and the results of the simulations, we find the velocity constrained density-temperature ratio method is the most robust and reliable in separating the sheath and magnetosphere plasmas.

The density-temperature ratio methods have a tendency to neglect some apparently sheath-like regions, and thus tailward velocity in the sheath is somewhat overestimated. This overestimation is consistent and predictable. Constraining the velocity significantly increases the growth rate in some, but not all cases, suggesting this is a useful method for identifying and characterizing rolled up, non-linear KHI vortices.

The entropy methods are the least reliable. Identified sheath regions include many intervals that to do not exhibit sheath-like characteristics despite having low entropy.

Thus the sheath velocity and density are much lower than expected. The reduced velocity shear and density parameters result in low growth rates. Constraining the tailward velocity universally increases the growth rate due to the severely reduced magnetospheric region (see green boxes in Figures 8 and 7), such that the sample size is too small to produce reliable parameters for the growth rate calculation. This may be an effect of the conservation of specific entropy across the boundary.

Use of the product of density and tailward velocity has inconsistent effects on the growth rate. Including mixed and ambiguous regions avoids the exclusion of relevant intervals seen in the other methods, but can also unpredictably affect the parameters used for the growth rate calculation. This is particularly pronounced in the simulation cases, where the identified values of physical parameters (density, temperature, etc.) for each distinct region approached the same value as the simulation progressed. This method appears less reliable than the velocity constrained density-temperature ratio when considering rolled-up KHI vortices.

- A comparison of two methods, the density-temperature ratio with and without constraints on the tailward velocity, is an effective way to identify KHI votices which have rolled-over.

Constraining the magnetospheric velocity for both the density-temperature ratio and entropy methods increased the final growth rate. In several cases this increase was an insignificant fraction of the growth rate, which we believe indicates MMS encountered a more linear stage of the KHI where very little if any magnetospheric plasma had been rolled-up in the vortex and accelerated downtail with the sheath. More significant increases in growth rate indicate a larger fraction of the previously identified magnetosphere was moving with the sheath, as expected for a non-linear rolled-up KH vortex. For only one event under either methodology (24 Oct 2016 for density-temperature ratio and 18 Feb 2016 for entropy) did the unitless growth rate decrease when velocity was constrained.

Ustable solid angles follow the same patterns as the unitless growth rate. When comparing the velocity constrained and unconstrained methods those events with insignificant increases in unstable solid angle match exactly the events with insignificant increases in growth rate. The same is true for cases with large increases and cases with decreases.

This further suggests the comparison of the methods with and without constraints on velocity are able consistently able to indicate if a KHI vortex has rolled over.

- The KHI is observed only when solar wind flow speeds are between 300 and 600 km/s. KHI growth rates are otherwise independent of the prevailing solar wind conditions.

Values of the unitless growth rate for each event using all 5 methods described in Sections 2.4.1 - 2.4.3 are presented in Table 5. Figure 14 then plots the mean unitless growth rates of all events as a function of (a) solar wind density, (b) temperature, (c) flow speed, (d) pressure, (e) IMF magnitude, and (f) Alfvén Mach number. Growth rates appear to be independent of most solar wind parameters, with the exception of solar wind flow speed. All of the observed events occurred when the solar wind was between 300 and 600 km/s. At flow speeds below 300 km/s the velocity shear is too low to satisfy the KHI onset conditions. At solar wind speeds above 600 km/s the compressibility of the plasma can stabalize the KHI [*Miura and Pritchett*, 1982]. Within this selection window, flow speed and growth rate are not correlated.

- The KHI is observed only when solar wind flow speeds are between 300 and 600 km/s. Unstable solid angles are otherwise independent of the prevailing solar wind conditions.

Table 6 lists the unstable solid angle of each KHI event calculated using the 5 methods described in Sections 2.4.1 - 2.4.3. The mean unstable solid angles for all events are plotted as function of (a) solar wind density, (b) temperature, (c) flow speed, (d) pressure, (e) IMF magnitude, and (f) Alfvén Mach number in Figure 15. As with the growth rates, unstable solid angles show no apparent correlation with solar wind conditions, with the exception of a selection window from 300 to 600 km/s flow speed. This confirms that KHI develop within an ideal plasma velocity range, such that the velocity is high enough (> 300 km/s) to satisfy the onset criteria, but not so high (> 600 km/s) as to produce high compressibility for typical magnetosheath plasma.

We note several of the observed events occur in apparently stable regions with very low growth rates; this does not preclude the observed events from being KHI. Convective instabilities like KHI dissipate energy stored in unstable regions and systems. As

529 **Table 5.** Unitless growth rates describe the speed at which the KHI develops as a fraction
530 of the local mean fast mode speed for each of the 19 MMS encounters. Parameters for each re-
531 gion both the sheath and magnetospheric regions were identified using 5 methods described in
532 Sections 2.4.1 - 2.4.3.

Event Date	n/T	n/T, v_x	S	S, v_x	nv_x	MEAN
08 Sep 2015	0.129	0.130	0.059	0.059	0.133	0.102
11 Oct 2015	0.018	0.018	0.031	0.032	0.004	0.021
15 Oct 2015	0.009	0.008	0.010	0.011	0.085	0.024
17 Oct 2015	0.027	0.037	0.014	0.018	0.068	0.033
18 Oct 2015	0.064	0.060	0.063	0.063	0.099	0.070
22 Dec 2015	0.001	0.020	0.002	0.005	0.044	0.014
11 Jan 2016	0.026	0.052	0.011	0.034	0.017	0.028
22 Jan 2016	0.014	0.012	0.004	0.009	0.029	0.014
05 Feb 2016	0.046	0.049	0.002	0.007	0.045	0.030
07 Feb 2016	0.004	0.019	0.010	0.019	0.012	0.013
18 Feb 2016	0.043	0.059	0.008	0.006	0.060	0.035
25 Feb 2016	0.021	0.045	0.008	0.039	0.023	0.027
26 Sep 2016	0.100	0.106	0.027	0.037	0.123	0.079
04 Oct 2016	0.043	0.080	0.005	0.041	0.078	0.049
10 Oct 2016	0.079	0.084	0.026	0.043	0.090	0.064
24 Oct 2016	0.013	0.007	0.001	0.001	0.011	0.007
04 Nov 2016	0.028	0.035	0.016	0.021	0.036	0.027
03 May 2017	0.155	0.169	0.165	0.171	0.134	0.159
11 May 2017	0.127	0.130	0.021	0.055	0.134	0.093

548 **Table 6.** The unstable solid angle is the percent of the total 4π solid angle which is unstable
549 to the development of the KHI. For each of the 19 MMS KHI encounters parameters for the
550 two sheath and magnetospheric regions are identified using each of the 5 methods described in
551 Sections 2.4.1 - 2.4.3.

Event Date	n/T	n/T, v_x	S	S, v_x	nv_x	MEAN
08 Sep 2015	6.93	6.98	3.83	3.84	6.97	5.71
11 Oct 2015	0.26	0.31	2.10	2.21	0.04	0.98
15 Oct 2015	0.07	0.06	0.25	0.30	5.48	1.23
17 Oct 2015	1.28	2.32	0.44	0.58	4.77	1.88
18 Oct 2015	5.68	6.12	5.39	5.39	7.62	6.04
22 Dec 2015	0.00	0.56	0.01	0.03	1.95	0.51
11 Jan 2016	0.73	2.65	0.15	1.27	0.22	1.00
22 Jan 2016	0.21	0.11	0.02	0.05	0.92	0.26
05 Feb 2016	5.21	5.56	0.02	0.14	3.66	2.92
07 Feb 2016	0.01	0.16	0.21	0.46	0.06	0.18
18 Feb 2016	5.24	7.72	0.11	0.07	5.88	3.80
25 Feb 2016	0.23	1.38	0.04	0.92	0.30	0.57
26 Sep 2016	7.47	8.22	2.35	3.37	9.64	6.21
04 Oct 2016	3.04	7.16	0.10	4.07	7.62	4.40
10 Oct 2016	7.14	7.73	2.44	4.19	7.56	5.81
24 Oct 2016	0.10	0.06	0.00	0.00	0.11	0.05
04 Nov 2016	1.35	1.83	0.80	1.08	1.93	1.40
03 May 2017	19.14	21.40	18.44	19.14	14.50	18.52
11 May 2017	12.14	12.53	0.65	6.24	12.54	8.82

559 excess energy is dissipated, the region becomes more stable, thus maximum instability
560 and growth rates occur just prior to the formation of the instability. KHI, by necessity,
561 are only observed after instability and growth rates have decreased from their maxima.
562 We believe those events occurring in apparently more stable regions are simply later in
563 development than faster growing KHI in less stable areas.

564 **Acknowledgments**

565 Funding for this work was provided by the National Science Foundation under grant num-
566 ber 1707521 and by NASA under grants numbers NNZ17AI50G and NNX16AF89G. Thanks
567 are owed to the entire MMS team, and especially to the FGM and FPI instrument groups.
568 MMS data was retrieved from the MMS Science Data Center at lasp.Colorado.edu/mms/sdc/public.
569 OMNI solar wind data is available from NASA Goddard Space Flight Center's Space Physics
570 Data Facility at omniweb.gsfc.nasa.gov.

571 ## References

572 Adamson, E., K. Nykyri, and A. Otto (2016), The Kelvin-Helmholtz Instability un-
573 der Parker-Spiral Interplanetary Magnetic Field Conditions at the Magnetospheric
574 Flanks, *Advances in Space Research*, *58*.

575 Axford, W., and C. Hines (1961), A Unifying Theory of High-Latitude Phenomena
576 and Geomagnetic Storms, *Canadian Journal of Physics*, *39*, 1433–1464.

577 Birn, J. (1980), Computer Studies of the Dynamic Evolution of the Geomagnetic
578 Tail, *Journ. of Geophys. Res.*, *85*, 1214–1222.

579 Burch, J. L., and T. D. Phan (2016), Magnetic Reconnection and the Dayside
580 Magnetopause: Advances with MMS, *Geophys. Res. Lett.*, *43*, 8327–8338, doi:
581 10.1002/2016GL069787.

582 Burch, J. L., T. E. Moore, R. B. Torbet, and B. L. Giles (2016), Magnetospheric
583 Multiscale Overview and Science Objectives, *Space Science Reviews*, *199*, 5–21,
584 doi:10.1007/s11214-015-0164-9.

585 Chandrasekhar, S. (1961), *Hydrodynamic and Hydromagnetic Stability*, Oxford Uni-
586 versity Press.

587 Chaston, C. C., M. Wilber, M. Fujimoto, M. L. Goldstein, M. Acuna, H. Rme,
588 and A. Fazakerley (2007), Mode Conversion of Anomalous Transport in Kelvin-
589 Helmholtz Vortices and Kinetic Alfvn Waves at Earth's Magnetopause, *Physical*

Review Letters, *99*.

Dimmock, A. P., and K. Nykyri (2013), The Statistical Mapping of Magnetosheath Plasma Properties Based on THEMIS Measurements in the Magnetosheath Interplanetary Medium Reference Frame, *Journ. of Geophys. Res.*, *118*, 4963–4876.

Dimmock, A. P., K. Nykyri, H. Karimbadi, A. Osmane, and T. I. Pulkkinen (2015), A statistical study into the spatial distribution and dawn-dusk asymmetry of dayside mangetosheath ion temperatures as a function of upstream solar wind conditions, *Journ. of Geophys. Res.*, *120*, 2767–2782, doi:10.1002/2014JA020734.

Eriksson, S., B. Lavraud, F. D. Wilder, J. E. Stawarz, B. L. Giles, J. L. Burch, W. Baumjohann, R. E. Ergun, P.-A. Lindqvist, W. Magnes, C. J. Pollock, C. R. Russel, Y. Saito, R. J. Strangeway, R. B. Torbert, D. J. Gershmann, Y. V. Khotyaintsev, J. C. Dorelli, S. J. Schwartz, L. Avanov, E. Grimes, Y. Vernisses, A. P. Sturner, T. D. Phan, G. T. Marklund, T. E. Moore, W. R. Paterson, and K. A. Goodrich (2016), Magnetospheric Multiscale Observations of Magnetic Reconnection Associated with Kelvin-Helmholtz Waves, doi:10.

Fairfield, D. H., A. Otto, T. Mukai, S. Kokubun, R. P. Lepping, J. T. Steinberg, A. J. Lazaurs, and T. Yamamoto (2000), Geotail observations of the Kelvin-Helmholtz instability at the equatorial magnetotail boundary for parallel northward fields, *Journ. of Geophys. Res.*

Foullon, C., C. J. Farrugia, A. N. Fazakerley, C. J. Owen, F. T. Gratton, and R. B. Torbert (2008), Evolution of Kelvin-Helmholtz Activity on the Dusk Flank Magnetopause, *Journ. of Geophys. Res.*, *113*, doi:10.1029/2008JA013175.

Gosling, J. T., M. F. Thomsen, S. J. Bame, and C. T. Russell (1986), Accelerated Plasma Flows at the Near-Tail Magnetopause, *Journ. of Geophys. Res.: Space Physics*, *91*, doi:10.1029/JA091iA03p03029.

Hasegawa, H., M. Fujimoto, K. Maezawa, Y. Saito, and T. Mukai (2003), Geotail observation of the dayside outer boundary region: Interplanetary magnetic field control and dawn-dusk asymmetry, *Journ. of Geophys. Res.*, *108*, doi:10.1029/2002JA009667.

Hasegawa, H., M. Fujimoto, T.-D. Phan, H. Réme, A. Balogh, M. W. Dunlop, C. Hashimoto, and R. TanDokoro (2004), Transport of solar wind into Earth's magnetosphere through rolled-up Kelvin-Helmholtz vortices, *Nature*, *430*, 755–758.

Hasegawa, H., M. Fujimoto, K. Takagi, Y. Saito, T. Mukai, and H. Réme (2006), Single-spacecraft detection of rolled-up Kelvin-Helmholtz vortices at the flank magnetopause, *Journ. of Geophys. Res.*, *111*, doi:10.1029/2006JA011728.

Hasegawa, H., A. Reino, A. Vaivads, Y. Khotyaintsev, M. Andre, T. K. M. Nakamura, L.-L. Teh, B. U. O. Sonnerup, S. J. Schwartz, Y. Seki, M. Fujimoto, Y. Saito, H. Reme, and P. Canu (2009), Kelvin-Helmholtz waves at the Earth's magnetopause: Multiscale development and associated reconnection, *Geophys. Res. Lett.*, *114*, doi:10.1029/2009JA014042.

Henry, Z. W., K. Nykyri, T. W. Moore, A. P. Dimmock, and X. Ma (2017), On the Dawn-Dusk Asymmetry of the Kelvin-Helmholtz Instability between 2007 and 2013, *Journ. of Geophys. Res.*, *122*, 11,888–11,900, doi:10.1002/2017JA024548.

Johson, J. R., C. Z. Cheng, and P. Song (2001), Signatures of Mode Conversion and Kinetic Alfvn Waves at the Magnetopause, *Geophys. Res. Lett.*, *28*.

Kavosi, S., and J. Reader (2015), Ubiquity of Kelvin-Helmholtz waves at the Earth's Magnetopause, *Nature Communications*.

King, J. H., and N. E. Papitashvili (2005), Solar Wind Spatial Sales in and Comparisons of Hourly Wind And ACE Plasma and Magnetic Field Data, *Journ. of Geophys. Res.*, *110*, doi:10.1029/2004JA010649.

Li, W., M. Andre, Y. V. Khotyaintsev, A. Vaivads, D. B. Graham, S. Toledo-Redondo, C. Norgren, P. Henri, C. Wang, B. B. Tang, B. Lavraud, Y. Vernisse, D. L. Turner, J. Burch, R. Torbet, W. Magnes, C. T. Russell, J. B. Blake, B. Mauk, B. Giles, C. Pollock, J. Fennell, A. Jaynes, L. A. Avanov, J. C. Dorellie, D. J. Gershman, W. R. Paterson, Y. Saito, and R. J. Strangeway (2016), Kinetic Evidence of Magnetic Reconnection due to Kelvin-Helmholtz Waves, *Geophys. Res. Lett.*, *43*, 5635–5643, doi:10.1002/2016GL069192.

Lin, D., C. Wang, W. Li, B. Tang, X. Guo, and Z. Peng (2014), Properties of Kelvin-Helmholtz Waves at the Magnetopause under Northward Interplanetary Magnetic Field: Statistical Study, *Journ. of Geophys. Res.: Space Physics*, *119*, 7485–7494, doi:10.1002/2014JA020379.

Ma, X., A. Otto, and P. Delamere (2014a), Interation of Magnetic Reconnection and Kelvin-Helmholtz Modes for Large Magnetic Shear: 1. Kelvin-Helmholtz Trigger, *Journ. of Geophys. Res.: Space Physics*.

Ma, X., A. Otto, and P. Delamere (2014b), Interation of Magnetic Reconnection and Kelvin-Helmholtz Modes for Large Magnetic Shear: 2. Reconnection Trigger, *Journ. of Geophys. Res.: Space Physics*.

Ma, X., P. Delamere, A. Otto, and B. Burkholder (2017), Plasma Transport Driven by the Three-Dimensional Kelvin-Helmholtz Instability, *Journ. of Geophys. Res.: Space Physics*, *122*.

Ma, X., P. Delamere, K. Nykyri, B. Burkholder, D. Neupane, and R. Rice (2019), Comparison Between Fluid Simulation With Test Particles and Hybrid Simultion for the Kelvin-Helmholtz Instability, *Journ. of Geophys. Res.: Space Physics*, *124*.

Merkin, V. G., J. G. Lyon, and S. G. Claudepierre (2013), Kelvin-Helmholtz Instability of the Magnetospheric Boundary in a Three-Dimensional Global MHD Simulation During Northward IMF Conditions, *Journ. of Geophys. Res.: Space Physics*, *118*, 5478–5496, doi:10.1002/jgra.50520.

Miura, A. (1984), Anomalous Transport by Magnetohydrodynamic Kelvin-Helmholtz Instabilities in the Solar Wind-Magnetosphere Interaction, *Journ. of Geophys. Res.*, *89*, 801–818.

Miura, A. (1987), Simulation of the Kelvin-Helmholtz Instability at the Magnetospheric Boundary, *Journ. of Geophys. Res.*, *92*, 3195–3206.

Miura, A., and P. L. Pritchett (1982), Nonlocal Stability of Analysis of the MHD Kelvin-Helmholtz Instability in a Compressible Plasma, *Journ. of Geophys. Res.*, *87*, 7431–7444.

Moore, T. W., K. Nykyri, and A. P. Dimmock (2016), Cross-scale energy transport in space plasmas, *Nature Physics*.

Moore, T. W., K. Nykyri, and A. P. Dimmock (2017), Ion-Scale Wave Properties and Enhanced Ion Heating Across the Low-Latitude Boundary Layer During Kelvin-Helmholtz Instability, *Journal of Geophysical Research: Space Physics*, *122*, 11,128–11,153, doi:10.1002/2017JA024591.

Nykyri, K. (2013), Impact of MHD Shock Physics on Magnetosheath Asymmetry and Kelvin-Helmholtz Instability, *Journal of Geophysical Reseach: Space Physics*, *118*, 5068–5081.

Nykyri, K., and A. Otto (2001), Plasma transport at the magnetopause boundary due to reconnection in Kelvin-Helmholtz vortices, *Geophys. Res. Lett.*, *28*, 3565–3568.

Nykyri, K., and A. Otto (2004), Influence of the Hall term on KH instability and reconnection inside KH vortices, *Ann. Geophys.*, *22*, 935–949.

Nykyri, K., A. Otto, , J. Büchner, B. Nikutowski, W. Baumjohann, L. M. Kistler, and C. Mouikis (2003), Equator-S Observations of Boundary Signatures: FTE's or Kelvin-Helmholtz Waves?, in *Earth's Low-Latitude Boundary Layer*, *Geophysical Monograph*, vol. 133, edited by P. T. Newell and R. Onsager, pp. 205–210, American Geophysical Union.

Nykyri, K., A. Otto, B. Lavraud, C. Mouikis, L. M. Kistler, A. Balogh, and H. Réme (2006), Cluster observations of reconnection due to the Kelvin-Helmholtz instability at the dawnside magnetospheric flank, *Ann. Geophys.*, *24*, 2619–2643.

Nykyri, K., A. Otto, E. Adamson, and J. Mumme (2011a), Cluster Observations of a Cusp Diamagnetic Cavity: Structure, Size, and Dynamics, *Journ. of Geophys. Res.*, *116*.

Nykyri, K., A. Otto, E. Adamson, and A. Tjulin (2011b), On the Origin of Fluctuation in the Cusp Diamagnetic Cavity, *Journ. of Geophys. Res.*, *116*, doi: 10.1029/2010JA015888.

Nykyri, K., X. Ma, A. Dimmock, C. Foullon, A. Otto, and A. Osmane (2017), Influence of Velocity Fluctuations on the Kelvin-Helmholtz Instability and its Associated Mass Transport, *Journ. of Geophys. Res.*, *122*, 9489–9512, doi: 10.1002/2017JA024374.

Nykyri, K., X. Ma, B. Burkholder, R. Rice, J. Johnson, E.-K. Kim, P. Delamere, A. Michael, K. Sorathia, D. Lin, S. Merkin, S. Fuselier, J. Broll, O. L. Contel, D. Gershman, I. Cohen, B. Giles, R. J. Strangeway, C. T. Russell, and J. Burch (2020), MMS Observations of the Multi-Scale Wave Structures and Parallel Electron Heating in the Vicinity of the Southern Exterior Cusp, *Journ. of Geophys. Res.: Space Physics*.

Otto, A. (1990), 3D Resistive MHD Computations of Magnetospheric Physics, *Computer Physics Communtications*, *59*, 185–195.

Otto, A., and D. H. Fairfield (2000), Kelvin-Helmholtz Instability at the Magnetotail Boundary: MHD Simulation and Comparison with Geotail Observations, *Journ. of Geophys. Res.*, *105*, 21,175–21,190.

Paschmann, G., B. O. . Sonnerup, I. Papamastorakis, G. Haerendel, S. J. Bame, J. R. Asbridge, J. T. Gosling, C. T. Russell, and R. C. Elphric (1979), Plasma

720 Acceleration at the Earth's Magnetopause: Evidence for Reconnection, *Nature*,
721 *282*, 243–246.
722 Pollock, C., T. Moore, A. Jacques, J. Burch, U. Gliese, Y. Saito, T. Omoto,
723 L. Avanov, A. Barrie, V. Coffey, J. Dorelli, D. Gershman, B. Giles, T. Ros-
724 nack, C. Salo, S. Yokota, M. Adrian, C. Aoustin, C. Auletti, S. Aung, V. Bigio,
725 N. Cao, M. Chandler, D. Chornay, K. Christian, G. Clark, G. Collinson, T. Cor-
726 ris, A. D. L. Santos, R. Devlin, T. Diaz, T. Dickerson, C. Dickson, A. Diekmann,
727 F. Diggs, C. Duncan, A. Figueroa-Vinas, C. Firman, M. Freeman, N. Galassi,
728 K. Garcia, G. Goodhart, D. Guererro, J. Hageman, J. Hanley, E. Hemminger,
729 M. Holland, M. Hutchins, T. James, W. Jones, S. Kreisler, J. Kujawaski, V. Lavu,
730 J. Lobell, E. LeCompte, A. Lukemire, E. MacDonald, A. Mariano, T. Mukai,
731 K. Narayanan, Q. Nguyan, M. Onizuka, W. Paterson, S. Persyn, B. Piepgrass,
732 F. Cheey, A. Rager, T. Raghuram, A. Ramil, L. Reichenthal, H. Rodriguez,
733 J. Rouzaud, A. Rucker, Y. Saito, M. Samara, J.-A. Sauvaud, D. Schuster,
734 M. Shappirio, K. Shelton, D. Sher, D. Smith, K. Smith, S. Smith, D. Steinfeld,
735 R. Szymkiewicz, K. Tanimoto, J. Taylor, C. Tucker, K. Tull, A. Uhl, J. Vloet,
736 P. Walpole, S. Weidner, D. White, G. Winkert, P.-S. Yeh, and M. Zeuch (), Fast
737 Plasma Investigation for Magnetospheric Multiscale, journal =.
738 Potter, D. (1973), *Computational Physics*, John Wiley and Sons.
739 Russell, C. T., B. J. Anderson, W. Baumjohann, K. R. Bromund, D. Dearborn,
740 D. Fischer, G. Le, H. K. Leinweber, D. Lenema, W. Magnes, J. D. Means, M. B.
741 Moldwin, R. Nakamura, D. Pierce, F. Plaschke, K. M. Rowe, J. A. Slavin, R. J.
742 Strangeway, R. Torbet, C. Hagen, I. Jernej, A. Valavanoglou, and I. Ricter ().
743 Sonnerup, B. U. O., and M. Scheible (1998), *Minimum and Maximum Variance*
744 *Analysis*, pp. 185–220, Inernational Space Science Institute.
745 Sonnerup, B. U. ., G. Paschmann, I. Papamastorakis, N. Sckopke, G. Haerendel,
746 S. J. Bame, J. R. Asbridge, J. T. Gosling, and C. T. Russell (), Evidence for Mag-
747 netic Field Reconnection at the Earth's Magnetopause, *Journ. of Geophys. Res.:*
748 *Space Physics*.
749 Sorathia, K. A., V. G. Merkin, A. Y. Ukhorskiy, R. C. Allen, K. Nykyri, and
750 S. Wing (2019), Solar Wind Ion Entry into the Magnetosphere During North-
751 ward IMF, *Journ. of Geophys. Res.: Space Physics*, *124*.

Stawarz, J. E., S. Eriksson, F. D. Wilder, R. E. Ergun, S. J. Schwartz, A. Pouquet, J. L. Burch, B. L. Giles, Y. Khotyaintsev, O. L. Contel, P.-A. Lindqvist, W. Magnes, C. J. Pollock, C. T. Russll, R. J. Strangeway, R. B. Torbert, L. A. Avanov, J. C. Dorelli, J. P. Eastwood, D. J. Gershman, K. A. Goodrich, D. M. Malaspina, G. T. Marklund, L. Mirioni, and A. P. Sturner (2016), Observations of Turbulence in a Kelvin-Helmholtz Event on 8 September 2015 by the Magnetospheric Multiscale mission, *Journ. of Geophys. Res.*, *121*, 11,021–11,034, doi:10.1002/10JA023458.

Taylor, M. G. G. T., B. Lavraud, C. P. Escoubet, S. E. Milan, K. Nykyri, M. W. Dunlop, J. A. Davies, R. H. W. Friedel, H. Frey, Y. V. Bogdanova, A. Asnes, H. Laasko, P. Trvincek, A. Masson, H. Opgenoorth, C. Vallat, A. N. Fazakerley, A. D. Lahiff, C. J. Owen, F. Pitout, Z. Pu, C. Shen, Q. G. Zong, H. Rme, J. Scudder, and T. L. Zhang (2008), The Plasma Sheet and Boundary Layers under Northward IMF: A Multi-point and Multi-instrument Perspective, *Advances in Space Research*, *41*, 1619–1629.

Taylor, M. G. G. T., H. Hasegawa, B. Lavraud, T. Phan, C. P. Escobet, M. W. Dunlop, Y. V. Bogdanova, A. L. Borg, M. Volwerk, J. Berchem, O. D. Constantinescu, J. P. Eastwood, A. Masson, H. Laakso, J. Soucek, A. N. Fazakerley, H. Frey, E. V. Panov, C. Shen, J. K. Shi, D. G. Sibeck, Z. Y. Pu, J. Wang, and J. A. Wild (2012), Spatial distribution of rolled up Kelvin-Helmholtz vortices at Earth's dayside and flank magnetopause, *Ann. Geophys.*

Torbet, R. B., C. T. Russell, w. Magnes, R. E. Ergun, P.-A. Lindqvist, O. LeContel, H. Vaith, J. Macri, S. Myers, D. Rau, J. Needell, B. King, M. Granoff, M. Chutter, I. Dors, G. Olsson, Y. V. Khotyaintsev, A. Eriksson, C. A. Kletzing, S. Bounds, B. Anderson, W. Baumjohann, M. Steller, K. Bromund, G. Le, R. Nakamura, R. J. Strangeway, H. K. Leinweber, S. Tucker, J. Westfell, D. Fisher, F. Plaschke, J. Porter, and K. Lappalainen (2016), The FIELDS Instrument Suite on MMS: Scientific Objectives, Measurements, and Data Products, *Space Science Reviews*, *199*, 105–135, doi:10.1007/s11214=014-0109-8.

Wilder, F. D., R. E. Ergun, S. J. Schwartz, D. L. Newman, S. Eriksson, J. E. Stawarz, M. V. Goldman, K. A. Goodrich, D. J. Gershman, D. M. Malaspina, J. C. Holmes, A. P. Sturner, J. L. Burch, R. B. Torbert, P.-A. Lindqvist, G. T. Marklund, Y. Khotyaintsev, R. J. Strangeway, C. T. Russel, C. J. Pollock, B. L.

Giles, J. C. Dorelli, L. A. Avanov, W. R. Patterson, F. Plaschke, and W. Magnes (2016), Observations of Large-Amplitude, Parallel, Electrostatic Waves Associated with the Kelvin-Helmholtz Instability by the Magnetospheric Multiscale Mission, *Geophys. Res. Lett.*, *43*, 8859–8866, doi:10.1002/2016GL070404.

Wing, S., J. R. Johnson, P. T. Newell, and C.-I. Meng (2005), Dawn-dusk asymmetries, ion spectra, and sources in the northward interplanetary magnetic field plasma sheet, *Journ. of Geophys. Res.*, *110*, doi:10.1029//2005JA011086.

Zhao, C., C. T. Russell, R. J. Strangeway, S. M. Petrinec, W. R. Paterson, M. Zhou, B. J. Anderson, W. Baumjohann, K. R. Bromund, M. Chutter, D. Fischer, G. Le, R. Nakamura, F. Plaschke, J. A. Slavin, R. B. Torbert, and H. Y. Wei (2016), Force Balance at the Magnetopause Determined with MMS: Application to Flux Transfer Events, *Geophys. Res. Lett.*, *43*, 11,941–11,947, doi:10.1002/2016GL071568.

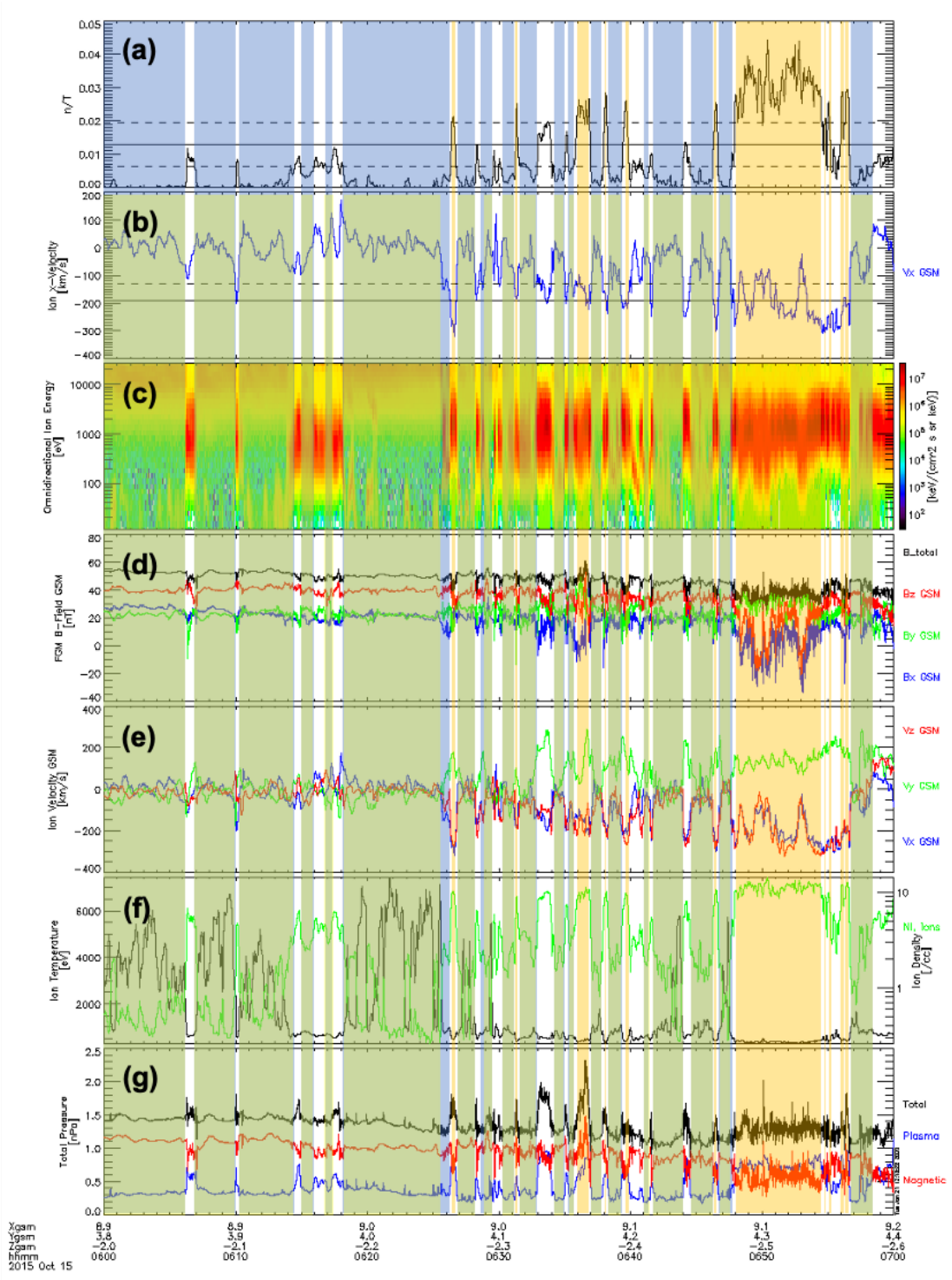

Figure 5. MMS observations of the (a) density-temperature ratio and (b) tailward velocity for the KHI event from 06:00 to 07:00 on 15 October 2015. Panels (c)-(g) are presented as in Figure 1 (a)-(e). Yellow boxes indicate magnetosheath regions, blue and green boxes are the magnetospheric regions for the velocity unconstrained and constrained methods respectively.

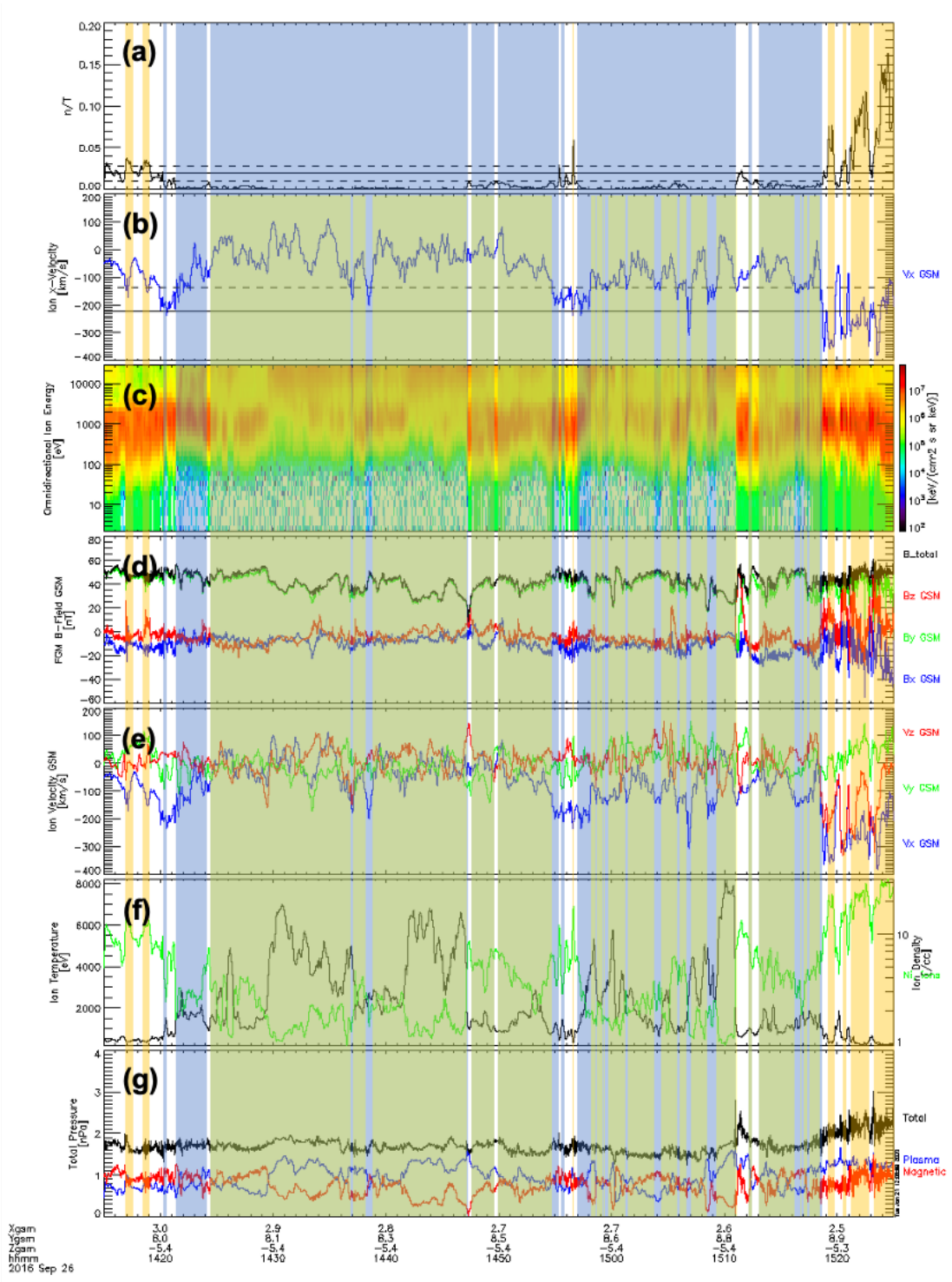

Figure 6. MMS observations, as in Figure 5 for the KHI event from 14:15 to 15:25 on 26 September 2016. Yellow boxes indicate magnetosheath regions, blue and green boxes are the magnetospheric regions for the velocity unconstrained and constrained methods respectively.

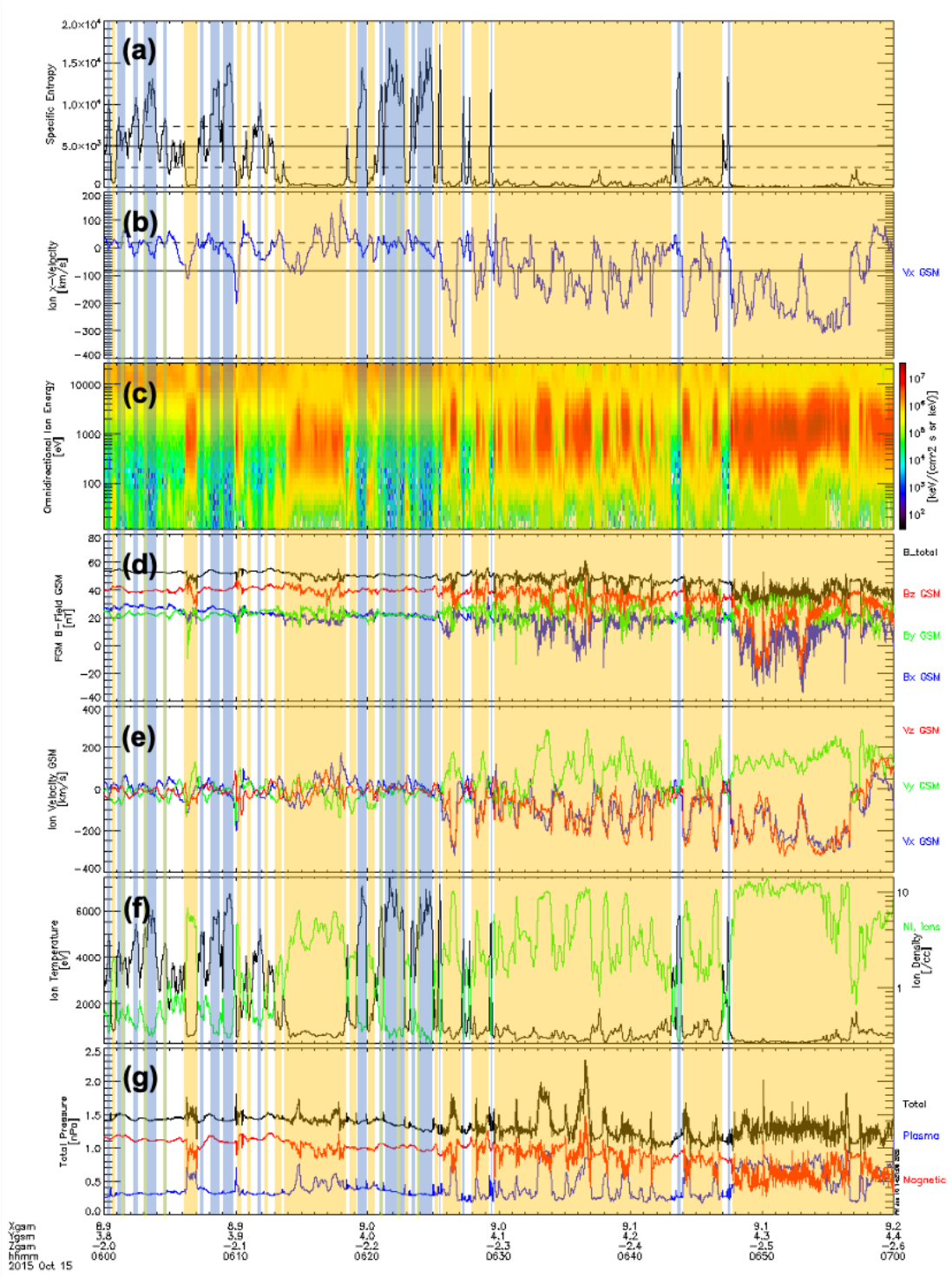

Figure 7. MMS observations of the (a) specific entropy and (b) tailward velocity for the KHI event from 06:00 to 07:00 on 15 October 2015. Panels (c)-(g) are presented as in Figure 1 (a)-(e). Yellow boxes indicate magnetosheath regions, blue and green boxes are the magnetospheric regions for the velocity unconstrained and constrained methods repsectively.

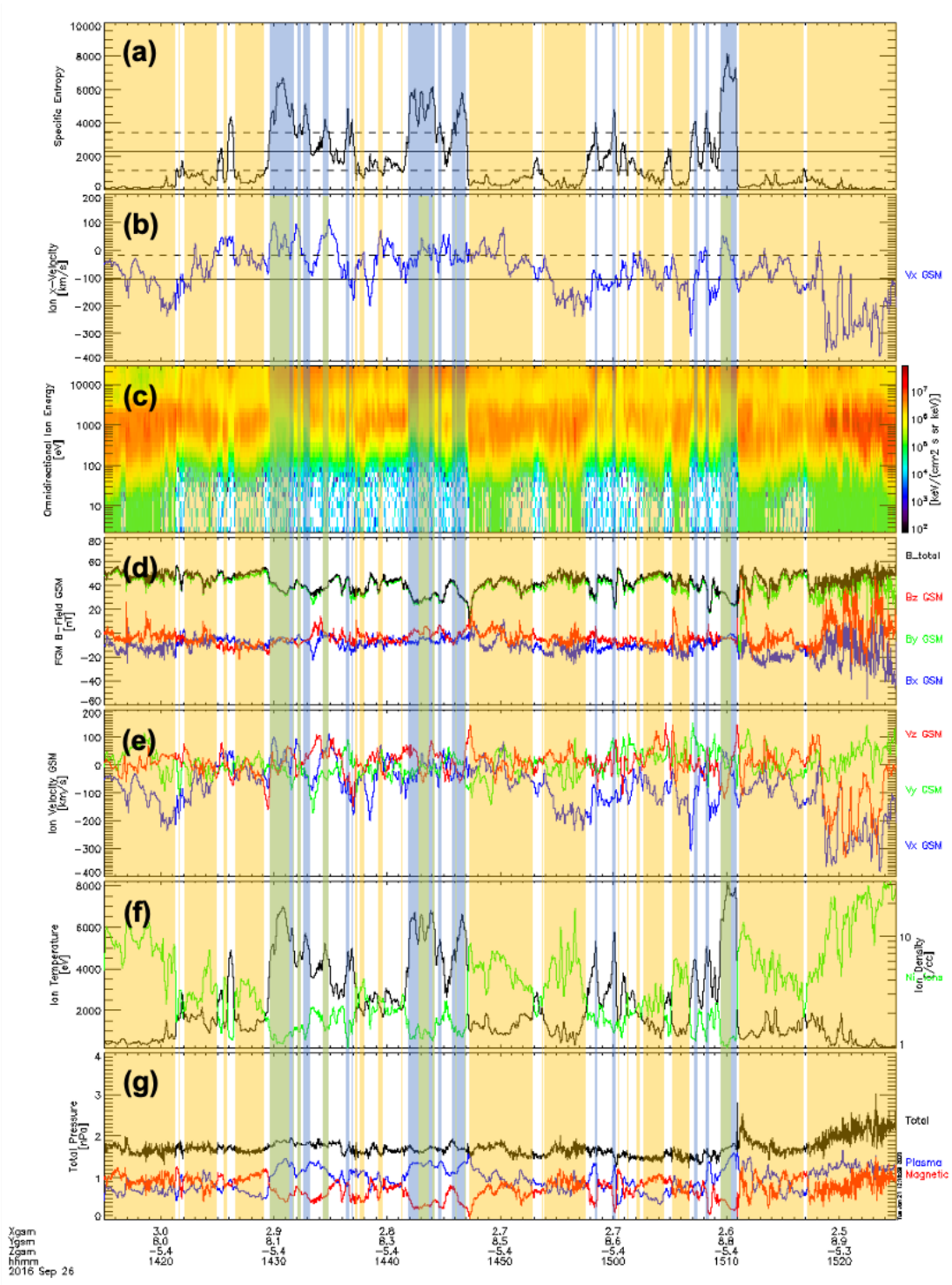

Figure 8. MMS observations as in Figure 7 for the KHI event from 14:15 to 15:25 on 26 September 2016. Yellow boxes indicate magnetosheath regions, blue and green boxes are the magnetospheric regions for the velocity unconstrained and constrained methods repsectively.

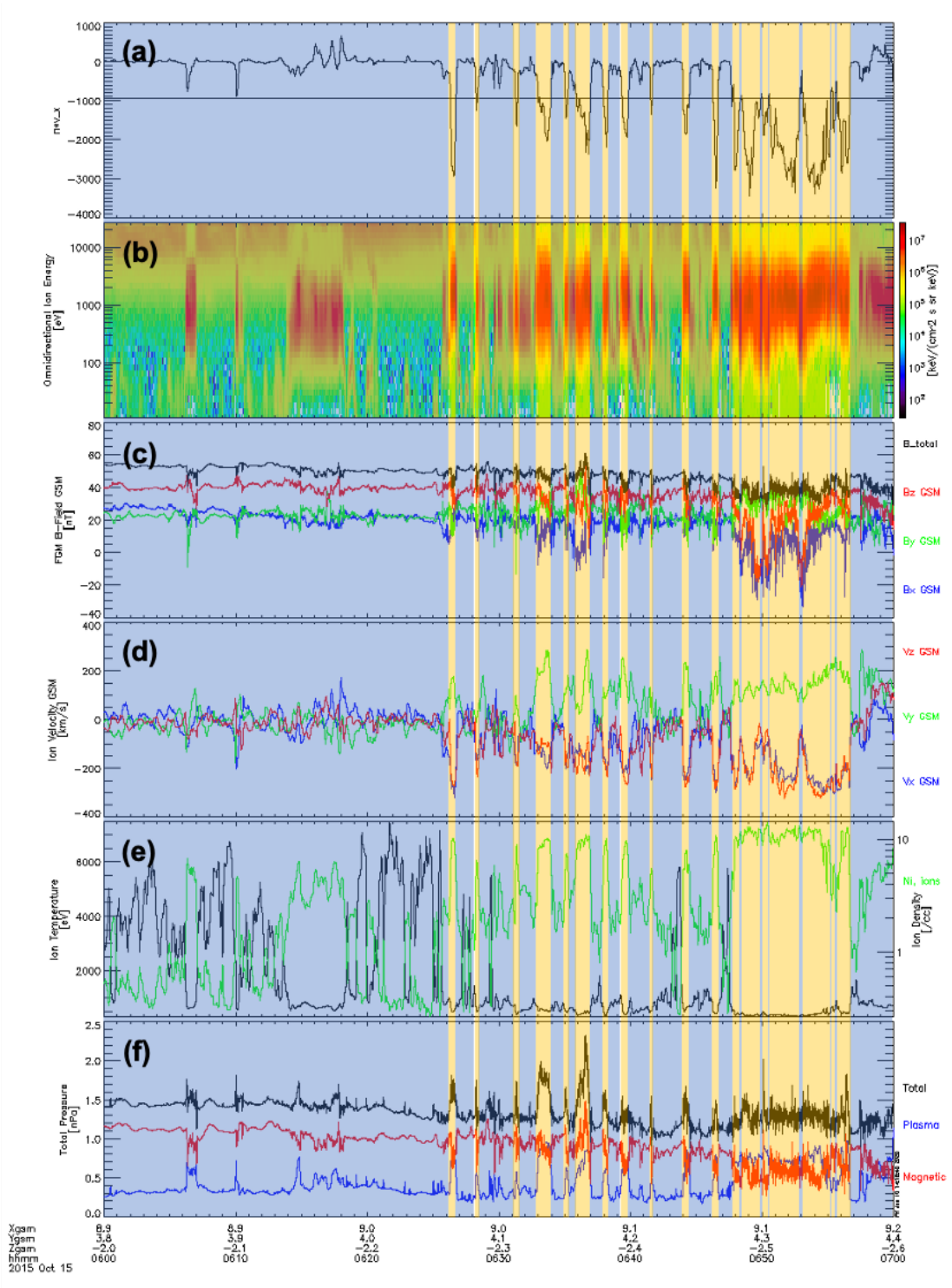

Figure 9. MMS observations of the (a) density-tailward velocity product for the KHI event from 06:00 to 07:00 on 15 October 2015. Panels (b)-(f) are presented as in Figure 1 (a)-(e). Yellow boxes indicate magnetosheath regions, blue boxes are the magnetospheric regions.

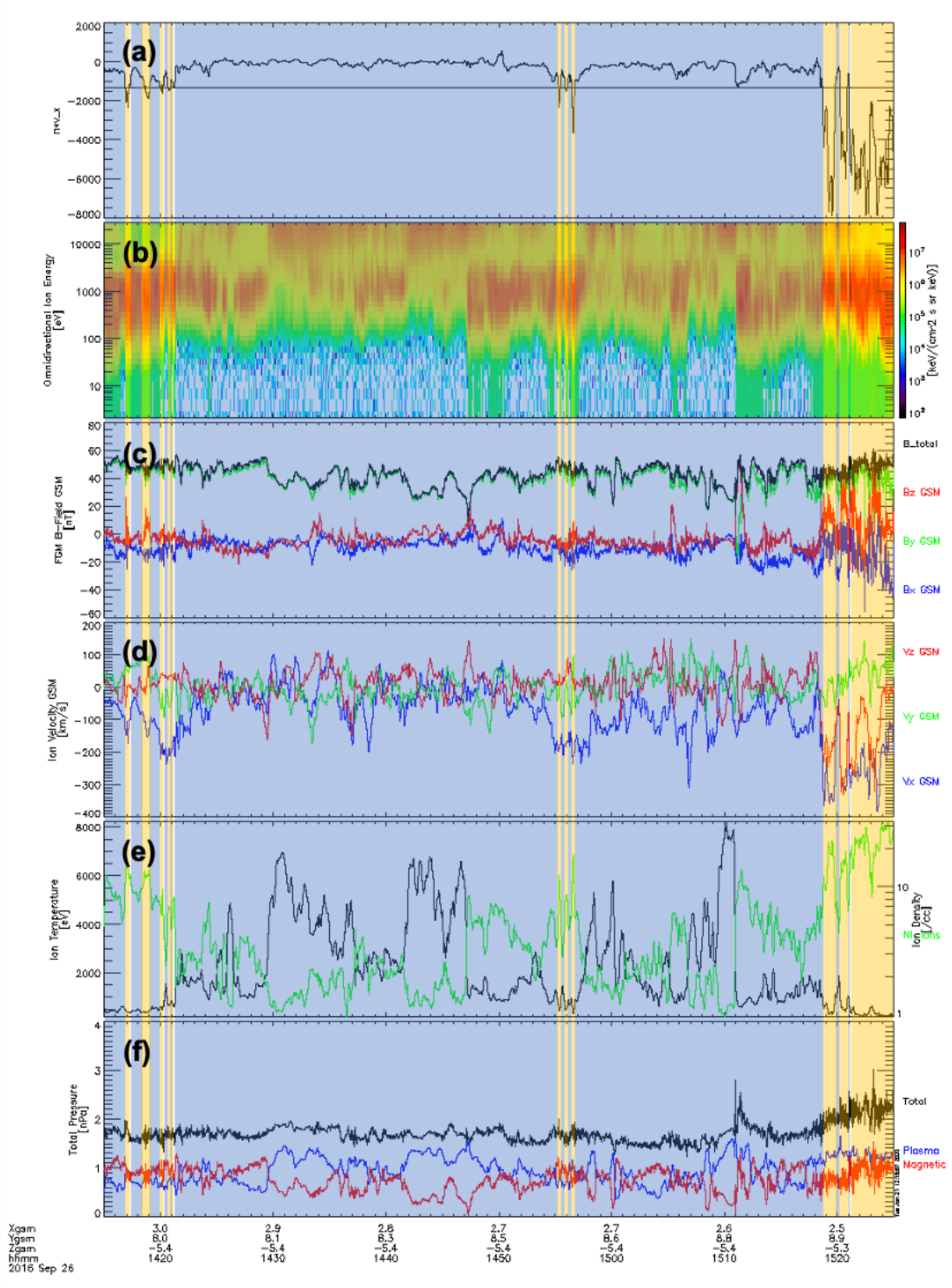

Figure 10. MMS observations as in Figure 9 for the KHI event from 14:15 to 15:25 on 26 September 2016. Yellow boxes indicate magnetosheath regions, blue boxes are the magnetospheric regions.

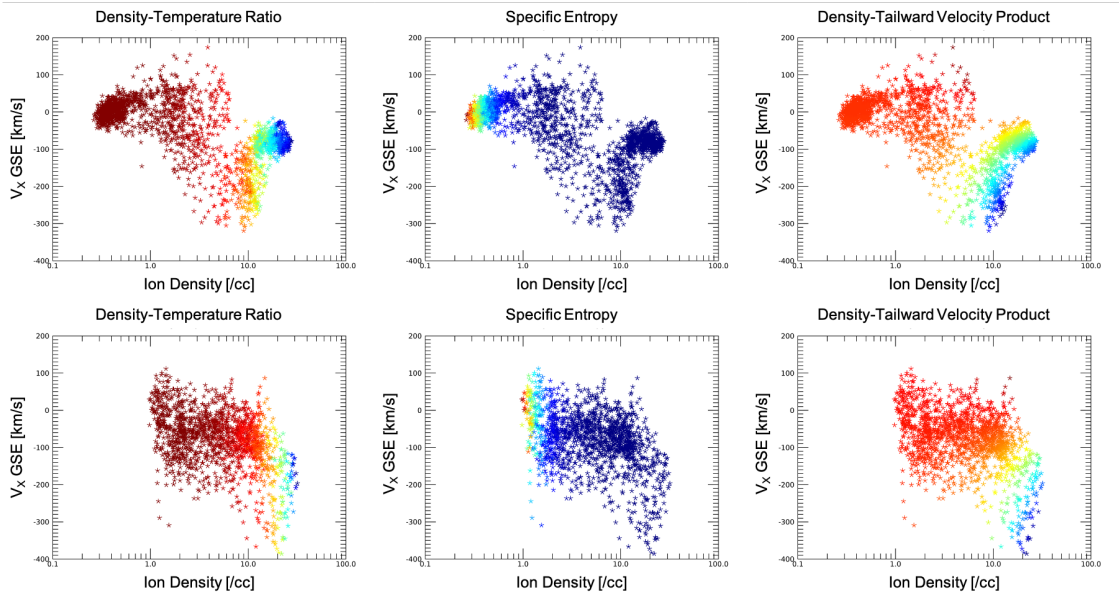

Figure 11. A comparison of MMS observed density (logarithmic scale) and tailward velocity for ions during (top) the 06:00-07:00 KH event on 15 October 2015 and (bottom) the 14:15-15:225 event on 26 September 2016. Color overlays indicate (left) density-temperature ratio, (center) specific entropy, and (right) density-tailward velocity product. Red points correspond to more sheath like characteristics and blue to more magnetosphere-like plasma.

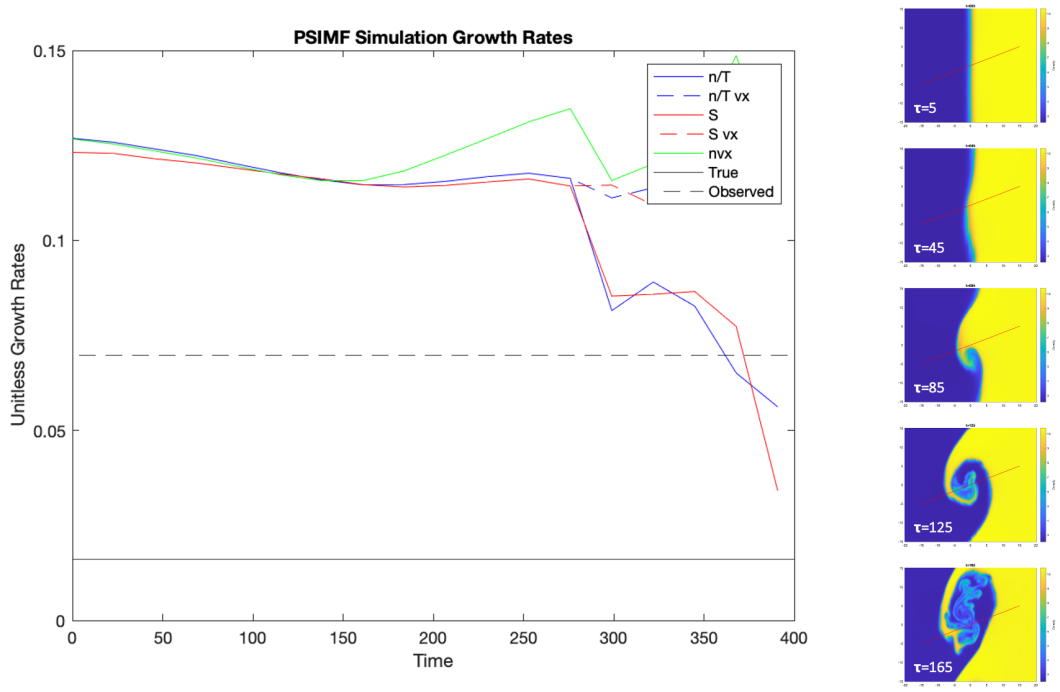

435 **Figure 12.** (Right) 2D MHD simulations of a dusk flank KHI occurring during Parker Spiral
436 IMF. Cuts, as indicated by the red line, were taken through the instability every 10 simulation
437 time steps and growth rates were calculated using all 5 methods and plotted as a function of time
438 (left). The true growth rate is indicated by the solid black line. The dashed black line indicates
439 the mean growth rate of the observational case on which the simulation is based.

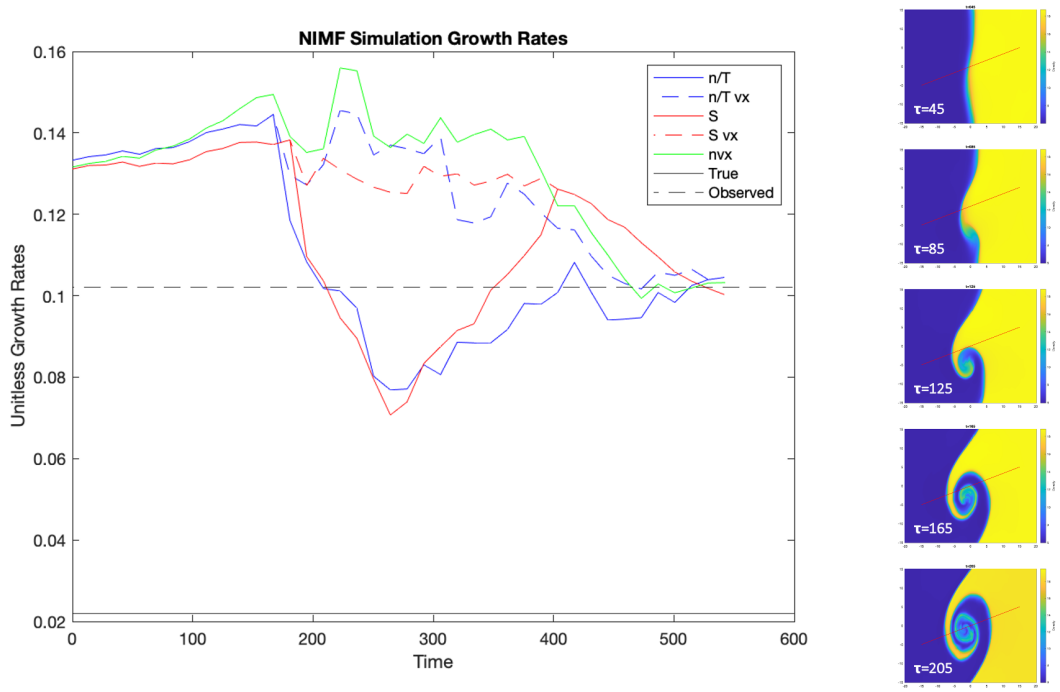

Figure 13. As Figure 12 for the 2D MHD simulation of a dusk flank KHI occurring under Northward IMF.

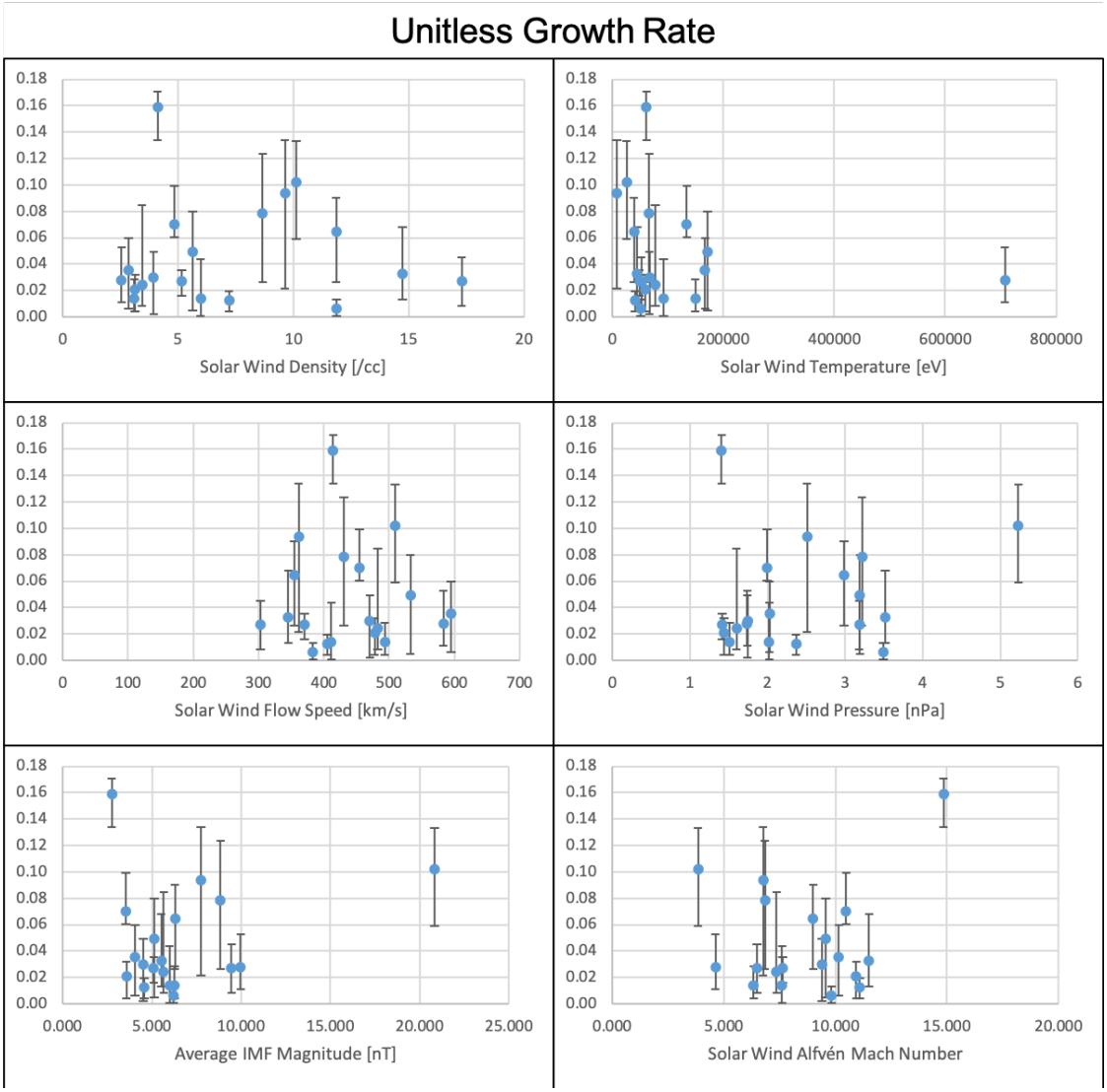

Figure 14. Unitless growth rates as a function of solar wind (a) density, (b) temperature, (c) flow speed, (d) pressure, (e) average IMF magnitude, and (f) Alfvén Mach number. Other than the window from 300-600km/s flow speed, growth rate is independent of solar wind parameters.

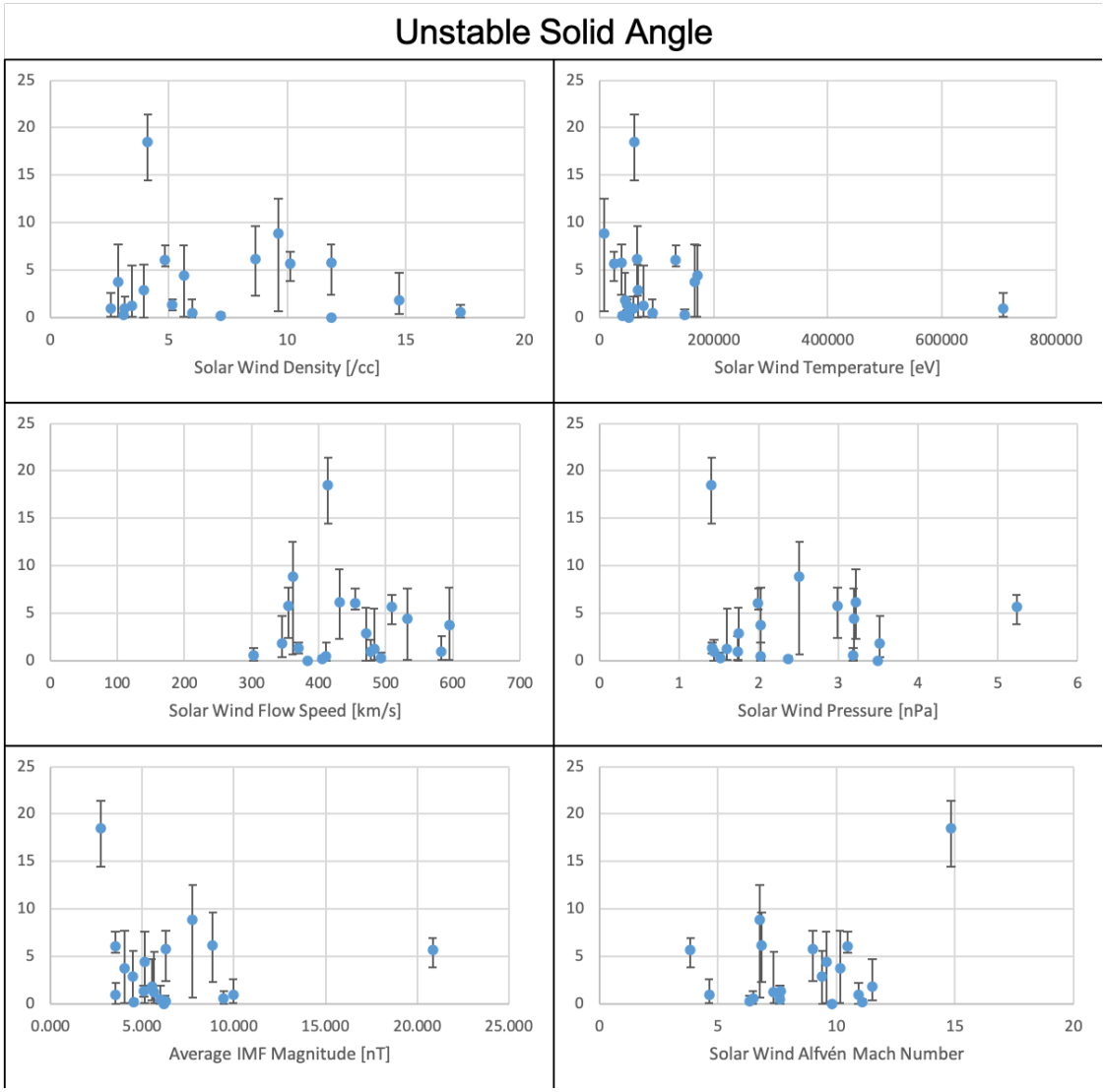

552 **Figure 15.** Unstable solid angles as a function of solar wind (a) density, (b) temperature, (c)
553 flow speed, (d) pressure, (e) average IMF magnitude, and (f) Alfvén Mach number. Other than
554 the window from 300-600km/s flow speed, unstable angle is independent of solar wind parame-
555 ters.